THE JOURNAL OF BIOLOGICAL CHEMISTRY VOL. 291, NO. 40, pp. 21296–21321, September 30, 2016

Architecture of the Human Mitochondrial Iron-Sulfur Cluster Assembly Machinery*

Received for publication, May 16, 2016, and in revised form, August 10, 2016 Published, JBC Papers in Press, August 12, 2016, DOI 10.1074/jbc.M116.738542

Oleksandr Gakh[‡1], **Wasantha Ranatunga**[‡1], **Douglas Y. Smith IV**[‡], **Eva-Christina Ahlgren**[§], **Salam Al-Karadaghi**[§], **James R. Thompson**[¶], **and Grazia Isaya**[‡2]

From the [‡]*Departments of Pediatric and Adolescent Medicine and Biochemistry Molecular Biology, Mayo Clinic Children's Research Center, and* [¶]*Department of Physiology and Biomedical Engineering, Mayo Clinic, Rochester, Minnesota 55905 and the* [§]*Center for Molecular Protein Science, Institute for Chemistry and Chemical Engineering, Lund University, P. O. Box 124, SE-221 00 Lund, Sweden*

Fe-S clusters, essential cofactors needed for the activity of many different enzymes, are assembled by conserved protein machineries inside bacteria and mitochondria. As the architecture of the human machinery remains undefined, we co-expressed in *Escherichia coli* the following four proteins involved in the initial step of Fe-S cluster synthesis: FXN^{42-210} (iron donor); [NFS1]·[ISD11] (sulfur donor); and ISCU (scaffold upon which new clusters are assembled). We purified a stable, active complex consisting of all four proteins with 1:1:1:1 stoichiometry. Using negative staining transmission EM and single particle analysis, we obtained a three-dimensional model of the complex with ~14 Å resolution. Molecular dynamics flexible fitting of protein structures docked into the EM map of the model revealed a $[FXN^{42-210}]_{24}\cdot[NFS1]_{24}\cdot[ISD11]_{24}\cdot[ISCU]_{24}$ complex, consistent with the measured 1:1:1:1 stoichiometry of its four components. The complex structure fulfills distance constraints obtained from chemical cross-linking of the complex at multiple recurring interfaces, involving hydrogen bonds, salt bridges, or hydrophobic interactions between conserved residues. The complex consists of a central roughly cubic $[FXN^{42-210}]_{24}\cdot[ISCU]_{24}$ sub-complex with one symmetric ISCU trimer bound on top of one symmetric FXN^{42-210} trimer at each of its eight vertices. Binding of 12 $[NFS1]_2\cdot[ISD11]_2$ sub-complexes to the surface results in a globular macromolecule with a diameter of ~15 nm and creates 24 Fe-S cluster assembly centers. The organization of each center recapitulates a previously proposed conserved mechanism for sulfur donation from NFS1 to ISCU and reveals, for the first time, a path for iron donation from FXN^{42-210} to ISCU.

Fe-S clusters are highly versatile cofactors that prokaryotic and eukaryotic cells utilize in many different proteins for a variety of functions. In yeast and animal cells, mitochondria are a main site of Fe-S cluster assembly (1), which involves highly conserved protein systems derived from the main bacterial Fe-S cluster assembly system (2, 3). All of these systems utilize IscU-type proteins as scaffolds upon which new Fe-S clusters are assembled and additional components, including the following: (i) pyridoxal phosphate-dependent cysteine desulfurases (bacterial IscS/yeast Nfs1/human NFS1), which in eukaryotes require a stabilizing binding partner (yeast Isd11/human ISD11) that provides elemental sulfur (4); (ii) members of the frataxin family (bacterial CyaY/yeast Yfh1/human FXN) that provide elemental iron (5–8) and also regulate the cysteine desulfurase activity (9, 10); and (iii) the electron donor chain formed by ferredoxin reductase and ferredoxin (11).

Biochemical studies have shown that Fe-S cluster assembly requires direct interactions among the proteins described above (6, 7, 11–13). In the specific case of the human system, two different isoforms of frataxin, FXN^{42-210} and FXN^{81-210}, participate in Fe-S cluster assembly using different modes of interaction with [NFS1]·[ISD11] and ISCU as well as different iron binding capacities (14). These isoforms are generated through sequential cleavage of the FXN protein precursor (FXN^{1-210}) by the mitochondrial processing peptidase upon import of FXN^{1-210} to the mitochondrial matrix (15–17). As determined by size-exclusion chromatography of normal human cell extracts, the native state of FXN^{42-210} is a monomer-oligomer equilibrium, whereas the native state of FXN^{81-210} is monomeric (7). Similarly in *Escherichia coli*, synthesis of recombinant FXN^{42-210} yields monomeric and oligomeric species (7), whereas synthesis of recombinant FXN^{81-210} yields monomer only (7, 12). *In vitro*, FXN^{81-210} binds to the pre-formed [NFS1]·[ISD11]·[ISCU] complex (7, 12, 18), whereas FXN^{42-210} oligomer forms stable contacts with [NFS1]·[ISD11] both in the absence or presence of ISCU (7). All of these interactions are iron-independent (7, 12, 18). Complexes containing native oligomeric FXN^{42-210}, NFS1, and ISCU could be isolated upon fractionation of normal human cell extracts by size-exclusion chromatography followed by co-immunoprecipitation (7, 19), underscoring the stability of these complexes. In contrast, native FXN^{81-210} was only recovered in fractions that contained no detectable NFS1 and only traces of ISCU (7, 19). A $[FXN^{81-210}]_2\cdot[NFS1]_2\cdot[ISD11]_4\cdot[ISCU]_2$ complex could be isolated from bacterial cells upon co-expression of all four components of the complex, and it could also be reconstituted *in vitro* from purified $[NFS1]_2\cdot[ISD11]_4\cdot[ISCU]_2$

---

* This work was supported in part by National Institutes of Health Grant AG15709-19 from NIA (to G. I. and J. T.). The authors declare that they have no conflicts of interest with the contents of this article. The content is solely the responsibility of the authors and does not necessarily represent the official views of the National Institutes of Health.

S This article contains supplemental Fig. S1 and Tables S1–S4

The atomic coordinates and structure factors (code 5KZ5) have been deposited in the Protein Data Bank (http://wwpdb.org/).

The EM map of the 3D reconstruction was deposited in the EMDB under the ID EMD-8293.

[1] Both authors contributed equally to this work.

[2] To whom correspondence should be addressed: Mayo Clinic, 200 First St. SW, Stabile 7-52, Rochester, MN 55905. Tel.: 507-266-0110; Fax: 507-266-9315; E-mail: isaya@mayo.edu.

complex and FXN$^{81-210}$ monomer. However, in both instances a large excess of FXN$^{81-210}$ monomer was required for complex formation (13, 18), which may explain why this complex could not be detected under native conditions in human cells (7, 19).

In the context of the complexes described above, both FXN$^{42-210}$ and FXN$^{81-210}$ stimulate the cysteine desulfurase activity of [NFS1]·[ISD11] in the presence of ISCU and L-cysteine *in vitro* (12, 19). Likewise, both isoforms support Fe-S cluster synthesis in the presence of [NFS1]·[ISD11], ISCU, L-cysteine, and ferrous iron under anaerobic conditions that prevent iron oxidation (7). However, under aerobic conditions that promote oxidation of Fe^{2+} to Fe^{3+}, FXN$^{81-210}$ monomer binds ≤1 iron equivalents (7, 13) and is unable to support Fe-S cluster synthesis (7). In contrast, under the same aerobic conditions, oligomeric FXN$^{42-210}$ chelates up to 10 molar eq of iron, and this ferric iron-loaded oligomer is able to support Fe-S cluster synthesis (7), similar to the oligomeric forms of *E. coli* and yeast frataxin (5, 6). The differences described above led us to propose that, in physiological conditions, FXN$^{81-210}$ may bind low levels of iron and support basal levels of Fe-S cluster assembly via transient interactions with the $[NFS1]_2$·$[ISD11]_4$·$[ISCU]_2$ complex, and that stable $[FXN^{42-210}]_n$·$[NFS1]_n$·$[ISD11]_n$·$[ISCU]_n$ complexes may provide a mechanism to increase the rate of Fe-S cluster assembly when the demand exceeds the low iron-binding capacity of FXN$^{81-210}$ (14). In agreement with the view that the two FXN isoforms have complementary roles, different disease states result from mutations that alter the FXN$^{81-210}$/FXN$^{42-210}$ molar ratio. FXN$^{42-210}$ is significantly more depleted than FXN$^{81-210}$ in patients with Friedreich ataxia (7), who have a progressive clinical course with death at a young age. Conversely, certain point mutations in MPP that cause FXN$^{81-210}$ depletion and FXN$^{42-210}$ accumulation are associated with a non-progressive form of cerebellar ataxia (17).

Based on structural analyses of complexes from bacteria (20–22) and yeast (8), a cartoon model for the $[FXN^{81-210}]_2$·$[NFS1]_2$·$[ISD11]_4$·$[ISCU]_2$ complex was proposed, showing a symmetric heterodimer formed by two [NFS1]·$[ISD11]_2$ sub-complexes with one ISCU subunit bound at each end, and one FXN$^{81-210}$ subunit bound in a pocket between each NFS1 and ISCU1 pair, which would result in the presence of one Fe-S cluster assembly site at each end of the complex (13). The mechanism of sulfur transfer to each of these sites involves a flexible loop of NFS1 containing the invariant cysteine residue, Cys-381, which is persulfurated through the cysteine desulfurase reaction (10, 12, 20, 21). Binding of FXN$^{81-210}$ to $[NFS1]_2$·$[ISD11]_4$·$[ISCU]_2$ accelerates persulfide formation on NFS1 and is also thought to induce a conformational change in ISCU that enhances the transfer of sulfur from NFS1 to Cys-138, the primary or main persulfide acceptor of ISCU (23–25) (note that Cys-138 corresponds to Cys-104 if the ISCU amino acid sequence is numbered starting from the mature protein N terminus instead of the precursor protein N terminus). Studies of the yeast system further suggest that sulfur-donation to ISCU may require conformational changes in NFS1 to (i) expose the NFS1 substrate-binding site, (ii) bring the flexible loop of NFS1 close to the substrate-binding site to enable formation of persulfurated Cys-381, and (iii) bring the NFS1 flexible loop close to the Fe-S cluster assembly site to enable sulfur transfer from persulfurated Cys-381 to ISCU (10, 26).

While the studies summarized above suggest a conserved path for sulfur donation from NFS1 to ISCU, the path for iron-donation remains undefined. In the context of the $[FXN^{81-210}]_2$·$[NFS1]_2$·$[ISD11]_4$·$[ISCU]_2$ complex it was proposed that one monomer of FXN$^{81-210}$ could bind in a pocket between the desulfurase and the scaffold through the frataxin iron-binding surface (13). However, binding of FXN$^{81-210}$ to $[NFS1]_2$·$[ISD11]_4$·$[ISCU]_2$ blocks the ability of FXN$^{81-210}$ to bind iron, which has been attributed to the fact that the frataxin iron-binding surface forms direct contacts with a positively charged patch on NFS1 (13). Whereas binding of FXN$^{81-210}$ to $[NFS1]_2$·$[ISD11]_4$·$[ISCU]_2$ also blocks the entry of iron into this complex, the addition of L-cysteine and the activation of the cysteine desulfurase activity restore iron entry even in the presence of bound FXN$^{81-210}$ (13). The mechanisms underlying these effects remain unexplained and the path for iron entry into the $[NFS1]_2$·$[ISD11]_4$·$[ISCU]_2$ complex is still unknown.

FXN$^{42-210}$, bacterial CyaY and yeast Yfh1 share a strong propensity to oligomerize *in vitro* (5, 7, 27, 28) and *in vivo* (7, 29, 30). We have shown that unlike CyaY or Yfh1, FXN$^{42-210}$ oligomerizes in an iron-independent manner, which involves the N-terminal region of the protein upstream of Ser-81 (7). Although Yfh1 oligomerization is iron-dependent (27), certain point mutations enable Yfh1 to oligomerize in an iron-independent manner just like FXN$^{42-210}$ (29, 31). Using one of these Yfh1 variants, Yfh1^{Y73A}, we were able to uncouple oligomerization of Yfh1 from iron binding and to study the complex formed by the apo-forms of Yfh1 and Isu1 (32). The structural model of the complex recapitulates the known mechanism for sulfur-donation from Nfs1 to Isu1 and also reveals a potential path for iron-donation from Yfh1 to Isu1 (32). The functional similarities between oligomeric Yfh1^{Y73A} and FXN$^{42-210}$, and in particular their common ability to store iron (29, 33) and to stimulate Fe-S cluster assembly (6, 7), suggest that oligomeric FXN$^{42-210}$ may be suitable to gain insight into the path for iron-donation in the human system. We therefore utilized a bacterial four-protein co-expression system to mimic the mitochondrial environment, and purified a stable and active macromolecular complex formed by FXN$^{42-210}$ with ISCU, NFS1 and ISD11. The architecture of the complex suggests a coordinated mechanism for the transfer of iron and sulfur to ISCU for the synthesis of [2Fe-2S] clusters.

Results

Isolation and Biochemical Characterization of Human Fe-S Cluster Assembly Complex—We previously reconstituted a functional $[FXN^{42-210}]_n$·$[NFS1]_n$·$[ISD11]_n$·$[ISCU]_n$ complex *in vitro* from independently expressed and purified FXN$^{42-210}$ oligomer, [NFS1]·[ISD11] sub-complex, and ISCU (7). In the same study, we detected similar complexes containing native FXN$^{42-210}$, NFS1, and ISCU in normal human cell extracts. In addition, in yeast cells expressing human frataxin precursor instead of yeast frataxin precursor, we detected complexes containing heterologous FXN$^{42-210}$ bound to endogenous Nfs1 and Isu1, which underscored the structural and functional conservation between the yeast and the human Fe-S cluster assembly systems (7). These previous data together with the high degree of conservation between prokaryotic and mitochondrial Fe-S cluster assembly systems (2, 3, 34) led us to hypothesize that simultaneous co-expression of FXN^{42-210}, NFS1, ISD11, and ISCU in *E. coli* might mimic the mitochondrial environment and yield similar complexes in sufficient quantities to enable structural studies. We therefore co-expressed the four proteins in *E. coli* as described under "Experimental Procedures." At the end of the protein expression phase, size-exclusion chromatography and SDS-PAGE analysis of the total bacterial cell extract revealed that similar levels of FXN^{42-210}, ISCU, and ISD11 were co-eluted with NFS1, which was present in large excess relative to the other three proteins (data not shown). Accordingly, nickel affinity chromatography of the total bacterial cell extract, utilizing a His_6 tag fused with the N terminus of NFS1, yielded one soluble pool containing all four proteins and a second pool containing NFS1 alone that was prone to aggregation likely due to the absence of ISD11 (data not shown) (35). Size-exclusion chromatography of the soluble nickel affinity chromatography pool, followed by affinity chromatography utilizing a Strep·Tag® II fused with the N terminus of FXN^{42-210}, yielded a soluble protein pool that once again contained all four proteins (Fig. 1*A*). As analyzed by size-exclusion chromatography and SDS-PAGE, the vast majority of the proteins in this pool were eluted together in one peak (Fig. 1*B*). To verify that the four proteins in the peak were bound to each other, the purified complex was incubated with DTSSP cross-linker, which can be cleaved by use of reducing agents. This sample was separated by size-exclusion chromatography, and the center of the peak containing the complex (fractions 56–60) was analyzed by SDS-PAGE in the presence or absence of β-mercaptoethanol. In the presence of the reducing agent, we detected the four individual proteins (Fig. 1*C*). In the absence of the reducing agent, we detected a single band that migrated in the high molecular mass region of the gel, with only traces of the individual proteins in the 45- to 11-kDa region of the gel, consistent with the presence of an almost completely cross-linked $[FXN^{42-210}]_n\cdot[NFS1]_n\cdot[ISD11]_n\cdot[ISCU]_n$ complex (Fig. 1*D*).

Purified complex was also incubated with a non-hydrolysable cross-linker, bis[sulfosuccinimidyl]suberate (BS^3),[3] and analyzed by size-exclusion chromatography. The chromatogram showed one peak with the same elution volume of the uncross-linked or DTSSP cross-linked complex, and SDS-PAGE in the presence of β-mercaptoethanol revealed a single band that migrated in the high molecular mass region of the gel, as observed with DTSSP cross-linker (Fig. 1, *E versus D*). The fact that the BS^3 cross-linked complex remained intact during reducing SDS-PAGE was consistent with our previous observation that interactions of oligomeric FXN^{42-210} with ISCU and/or [NFS1]·[ISD11] can occur under reducing conditions *in vitro* (6, 7). To verify this further, purified complex was incubated for 1 h in the presence of 5 mM β-mercaptoethanol and subsequently purified by size-exclusion chromatography in TN150 buffer containing 5 mM β-mercaptoethanol. As analyzed by SDS-PAGE, reducing conditions during size-exclusion chromatography resolved high molecular weight species present in fractions 38–50; however, the elution profile of the complex was indistinguishable regardless of the presence of the reducing agent (Fig. 1, *B versus F*). After another size-exclusion chromatograph of the complex in the absence of reducing agent, we analyzed fractions 56–60 by reducing and non-reducing SDS-PAGE. In non-reducing conditions, we detected the four protein components of the complex and only faint bands in the region of the gel >94 kDa (Fig. 1*G*), where the whole complex migrates (see Fig. 1, *D* and *E*). In addition, there were three bands that were not present under reducing conditions (Fig. 1*G*). Mass spectrometry identification of proteins in each of these three bands (supplemental Table S1) indicated that band* and band** most likely represent faster migrating forms of ISCU and NFS1, respectively, resulting from *intra*-molecular disulfide bonds that make each protein more compact. The data further indicated that band*** most likely represents a slower migrating form of FXN^{42-210}, probably a dimer given the apparent molecular mass of ~46 kDa (Fig. 1*G*), which may result from an *inter*-molecular disulfide bond between FXN^{42-210} subunits. It is unlikely that *inter*-molecular disulfide bonds are required to stabilize oligomeric FXN^{42-210} as the protein contains only one Cys residue, Cys-50, which is outside of the N-terminal region necessary and sufficient for oligomerization (residues 56–78) (36). Therefore, based on all of these results together, we concluded that disulfide bonds do not play a significant role in the formation or stability of the $[FXN^{42-210}]_n\cdot[NFS1]_n\cdot[ISD11]_n\cdot[ISCU]_n$ complex.

Protein staining and densitometry of SDS-polyacrylamide gels suggested the complex might consist of approximately equimolar amounts of FXN^{42-210}, ISCU, and ISD11 and an apparently 2–3-fold excess of NFS1 (Fig. 1, *A* and *B*). The fact that NFS1 appeared to be present in excess of ISD11 was in contrast with previous observations that the yeast orthologues, Nfs1 and Isd11, form a complex that contains stoichiometric amounts of each protein in a 1:1 ratio (37, 38). Given that NFS1 is significantly larger than ISD11 (~45 kDa *versus* ~11 kDa), we considered the possibility that equimolar levels of NFS1 might correspond to ~4 times higher local protein concentrations inside the gel, resulting in enhanced stainability of NFS1 compared with ISD11 (39). To avoid this issue, we determined the stoichiometry of the four proteins in the complex via amino acid analysis of fractions 58 and 59. We compared different predicted amino acid compositions of the complex to the experimentally measured composition, and we then calculated the variation for each amino acid and the total % variation (Table 1). Different predicted amino acid compositions of the complex were based on the assumption that the complex might be made up of FXN^{42-210}, ISCU, NFS1, and ISD11 in a 1:1:1:1 or 1:1:2:1 or 1:1:1:2 or 2:1:1:1 or 1:2:1:1 molar ratio. Independent amino acid analysis of fractions 58 and 59 yielded almost identical experimental compositions, the average of which was used in the calculations. The total % variation for the 1:1:1:1, 1:1:2:1,

---

[3] The abbreviations used are: BS^3, bis[sulfosuccinimidyl]suberate; FXN and Yfh1, human and yeast frataxin; ISCU and Isu1, human and yeast iron-sulfur cluster assembly scaffold protein; NFS1 and Nfs1, human and yeast cysteine desulfurase 1; ISD11 and Isd11, human and yeast cysteine desulfurase stabilizing partner; FSC, Fourier shell correlation; BSA, buried surface area; FDR, false discovery rate; RDE, resolution-dependent error; PDB, Protein Data Bank; DTSSP, dithiobis(sulfosuccinimidyl propionate).

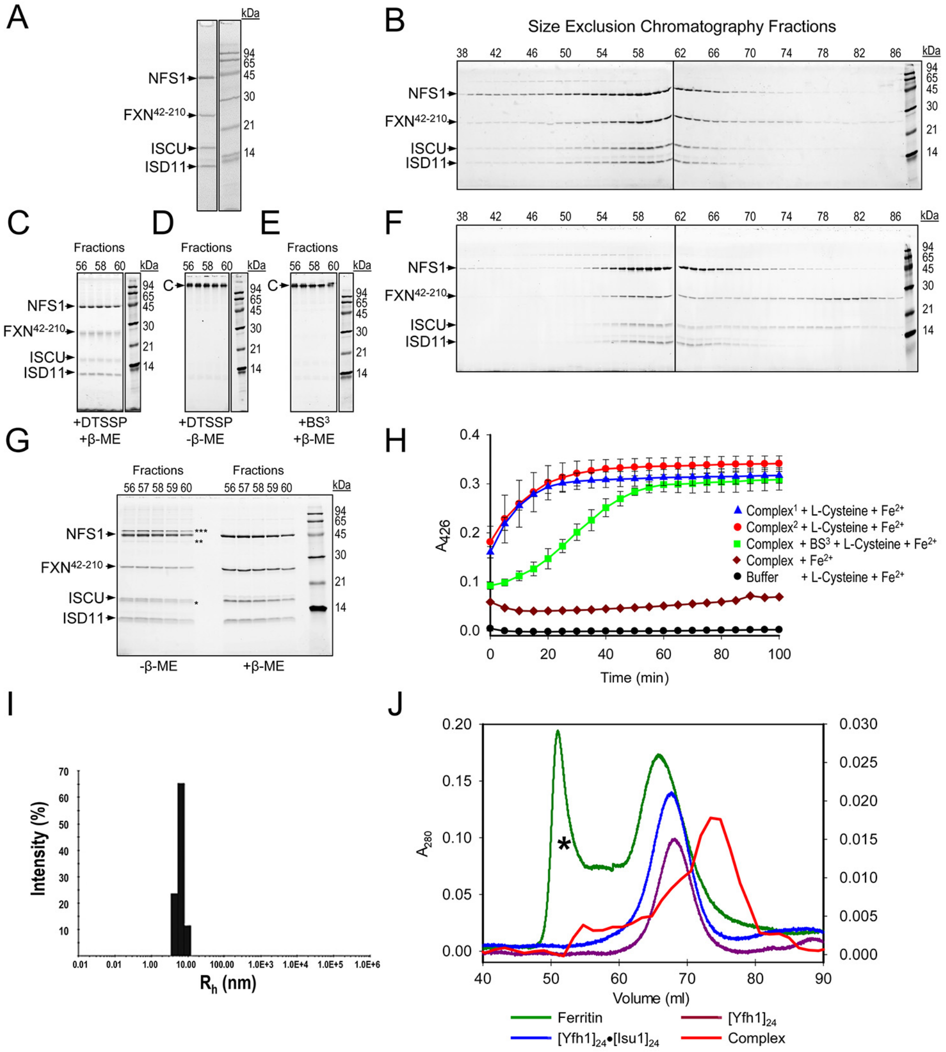

FIGURE 1. **Co-expression of human FXN$^{42-210}$, NFS1, ISD11, and ISCU proteins in *E. coli* yields a stable and active four-protein complex.** *A*, histidine-tagged NFS1 was co-expressed in *E. coli* with ISD11, ISCU, and streptavidin-tagged FXN$^{42-210}$, and a complex containing all four proteins was purified as described under "Experimental Procedures." *B*, Sephacryl S-300 size-exclusion chromatography and SDS-PAGE analysis of purified complex. *C–E*, complex eluted from the StrepTrap^{TM} HP affinity column was treated with DTSSP (*C* and *D*) or BS^3 (*E*) cross-linker and purified by size-exclusion chromatography, after which fractions 56–60 were analyzed by SDS-PAGE in the presence (*C* and *E*) or absence (*D*) of the reducing agent β-mercaptoethanol (*β-ME*). *F*, complex eluted from the StrepTrap^{TM} HP affinity column was incubated for 1 h in the presence of 5 mM β-mercaptoethanol, purified by size-exclusion chromatography in TN150 buffer containing 5 mM β-mercaptoethanol, and analyzed by SDS-PAGE. *G*, after size-exclusion chromatography in the absence of reducing agent (*B*), fractions 56–60 were analyzed by SDS-PAGE in the absence or presence of β-mercaptoethanol. *Asterisks* denote protein bands that are only observed under non-reducing conditions (see supplemental Table S1 for details). *H*, indicated complex preparations were tested for their ability to catalyze Fe-S cluster assembly; *Complex*^{1} and *Complex*^{2} denote complex after the third and the last purification steps. Assays were performed anaerobically in the presence of 5 μM complex, 1 mM L-cysteine, 50 μM Fe^{2+} as described under "Experimental Procedures." Each of the plots shows the mean ± S.D. of three independent measurements with two different complex preparations. *I*, dynamic light scattering measurements were performed on BS^3-cross-linked complex freshly eluted from the size-exclusion chromatography column, and the hydrodynamic radius (R_h) was obtained as described under "Experimental Procedures." *J*, elution volumes of the human complex (*Complex*) and the indicated protein complexes analyzed by Sephacryl S-300 size-exclusion chromatography. *Asterisk* denotes ferritin dimer. Although the predicted molecular mass of the human complex (~2 MDa) is greater than that of ferritin (700–800 kDa due to iron content), these two complexes are eluted according to their similar dimensions (40). The fact that the human complex elutes slightly later than ferritin may also be due to retardation through weak adsorption to the gel.

1:1:1:2, 2:1:1:1, and 1:2:1:1 molar ratios was 1.2, 32.9, 8.4, 17.6, and 13.2% (Table 1 and not shown for the last two ratios). These data supported a $[\text{FXN}^{42-210}]_n\cdot[\text{NFS1}]_n\cdot[\text{ISD11}]_n\cdot[\text{ISCU}]_n$ complex containing stoichiometric amounts of its four-protein components in a 1:1:1:1 molar ratio.

We also measured levels of bound iron in the complex using fractions 58 and 59 and detected only traces of iron, corresponding to 0.05 ± 0.001 atoms of iron present per subunit of the complex or ~1 atom of iron per complex, calculated assuming that one subunit of the complex corresponds to one $[\text{FXN}^{42-210}]\cdot[\text{NFS1}]\cdot[\text{ISD11}]\cdot[\text{ISCU}]$ heterotetramer and that there are 24 such subunits in the complex as described below. This finding is consistent with our previous observation that oligomeric FXN$^{42-210}$ forms complexes with [NFS1]·[ISD11] and ISCU in an iron-independent manner (7).

Finally, to assess the suitability of using chemical cross-linking to probe the complex structure, we assessed the ability of the uncross-linked and BS^3 cross-linked complex to catalyze Fe-S cluster formation in the presence of L-cysteine and Fe^{2+} after both the streptavidin affinity chromatography and the

TABLE 1

Amino acid analysis of human four-protein complex

The experimental amino acid composition of purified complex, as determined via amino acid analysis, is compared with three expected compositions based on the three potential FXN$^{42-210}$/ISCU/NFS1/ISD11 molar ratios shown. For each molar ratio, the variation between the experimental and expected number of each amino acid and the total % variation is shown. Sixteen amino acids were quantified; tryptophan and cysteine are degraded by the hydrolysis process, and asparagine and glutamine are detected as aspartic and glutamic acid, respectively (75).

Amino Acid	Experimental composition (no. of amino acids)	FXN-ISCU-NFS1-ISD11 (1:1:1:1)		FXN-ISCU-NFS1-ISD11 (1:1:2:1)		FXN-ISCU-NFS1-ISD11 (1:1:1:2)	
		Expected composition (no. of amino acids)	Variation	Expected composition (no. of amino acids)	Variation	Expected composition (no. of amino acids)	Variation
Ala	70.8	63	−7.8	93	22.2	69	−1.8
Arg	51.0	49	−2.0	76	25.0	62	11.0
Asp	78.9	72	−6.9	102	23.1	82	3.1
Glu	96.8	85	−11.8	131	34.2	93	−3.8
Gly	62.3	60	−2.3	92	29.7	62	−0.3
His	25.8	28	2.2	47	21.2	29	3.2
Ile	44.6	46	1.4	76	31.4	52	7.4
Leu	75.7	76	0.3	111	35.3	83	7.3
Lys	55.1	61	5.9	82	26.9	67	11.9
Met	21.6	24	2.4	39	17.4	27	5.4
Phe	18.3	17	−1.3	24	5.7	19	0.7
Pro	30.4	35	4.6	55	24.6	37	6.6
Ser	60.9	67	6.1	104	43.1	71	10.1
Thr	46.6	45	−1.6	65	18.4	49	2.4
Tyr	29.7	30	0.3	45	15.3	35	5.3
Val	58.5	59	0.5	91	32.5	66	7.5
Total amino acids	827.2	817	−10.2	1233	405.8	903	75.8
Total percent variation			1.20%		32.90%		8.40%

size-exclusion chromatography purification steps, and we detected very similar activity in both samples (Fig. 1*H*). Complex cross-linked with BS^3 was also able to catalyze Fe-S cluster formation with slower kinetics but a similar final yield as compared with the uncross-linked complex (Fig. 1*H*). Chemical cross-linking data later indicated that the slower kinetics of the cross-linked complex probably reflected cross-linking of flexible structural elements involved in Fe-S cluster assembly (see Fig. 14*F*).

Dynamic light scattering of pooled fractions 56–60 revealed a hydrodynamic radius (R_h) of 7.4 ± 0.3 nm with unimodal distribution (Fig. 1*I*). We measured and compared the R_h and elution profiles of the $[\mathrm{FXN}^{42-210}]_n\cdot[\mathrm{NFS1}]_n\cdot[\mathrm{ISD11}]_n\cdot[\mathrm{ISCU}]_n$ complex with those of previously characterized globular complexes, including the $\mathrm{Yfh1}^{\mathrm{Y73A}}$ 24-mer ($R_h = 7.6 \pm 0.5$) (31), the $[\mathrm{Yfh1}^{\mathrm{Y73A}}]_{24}\cdot[\mathrm{Isu1}]_{24}$ complex ($R_h = 7.2 \pm 0.2$) (32), and the horse spleen ferritin 24-mer ($R_h = 7.5 \pm 0.2$). The four complexes were eluted with similar retention volumes between ~66 and 74 ml (measured between the ferritin and the human complex peaks in Fig. 1*J*), a result consistent with their similar R_h (40) and with the size-exclusion pore dimension of the Sephacryl S-300 gel matrix (~13 nm) (41).

EM Single Particle Reconstruction of the $[\mathit{FXN}^{42-210}]_n\cdot[\mathit{NFS1}]_n\cdot[\mathit{ISD11}]_n\cdot[\mathit{ISCU}]_n$ *Complex*—Uranyl acetate staining of aliquots from pooled fractions 56–60 revealed roughly globular shapes with a diameter of 15.3 ± 0.7 nm (average of 351 particles) (Fig. 2*A* and not shown), consistent with the R_h measured by dynamic light scattering and the behavior of the complex in size-exclusion chromatography. These data together suggested we were dealing with an overall homogeneous population of roughly globular particles. We took EM images of the uranyl acetate-stained particles at a magnification of 115,000 with an Å/pixel ratio of 1.034. We collected 4124 particles and used the ~786 best particles to generate reference free class averages using the EMAN2 software package (Fig. 2*A*) (42). Although all class averages exhibited similar globular shape and diameter of ~15 nm, each class exhibited unique structural details (Fig. 2*A*), suggesting the complex adsorbed to the carbon film of the EM grids with different orientations. Given the high degree of conservation between the yeast and the human systems (7, 15), and based on the measured 1:1:1:1 stoichiometry of the complex, we hypothesized that the architecture of the human four-protein complex might be similar to the recently reported architecture of the $[\mathrm{Yfh1}]_{24}\cdot[\mathrm{Isu1}]_{24}\cdot[\mathrm{Nfs1}]_{24}$ complex, which has 432 symmetry (PDB code 5T0V) (32). Therefore, initial 3D models were generated from the class averages without or with 432 symmetry applied (Fig. 2*A*). Refinement of these models using the larger set of ~4124 particles yielded models of similar globular shape (Fig. 2, *B–D* and *E–G*). Then, structure factors were calculated from the EM density map of the refined 3D model without symmetry applied, and a self-rotation function was obtained (43). Similar calculations were completed using the EM density map of the refined 3D model with 432 symmetry applied. These data revealed the presence of 432 symmetry in both models (Fig. 2, *H versus I*). Using the 0.143 cutoff (44), the FSC plots indicated resolutions of 15.0 and 13.5 Å, respectively, for the model without and with symmetry applied (Fig. 2, *J* and *K*). Resolutions

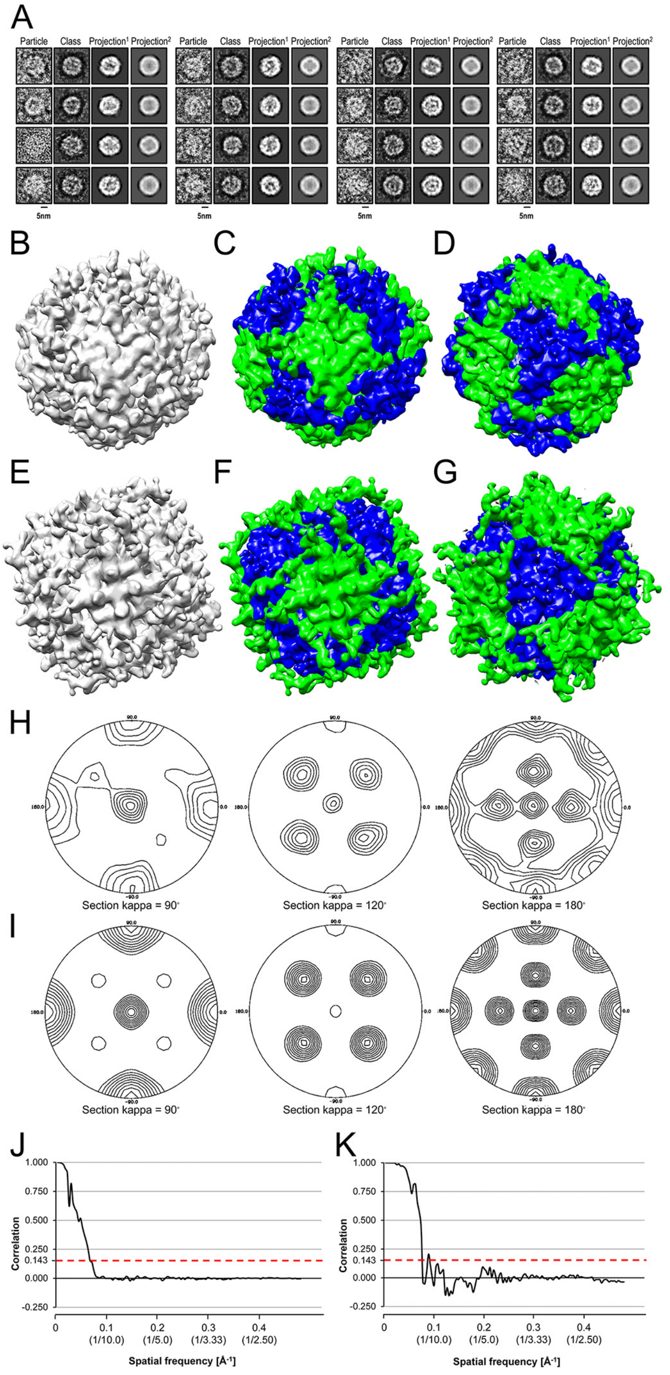

FIGURE 2. **Transmission EM and single particle analysis of human four-protein complex.** *A*, electron micrographs of purified uranyl acetate-stained complex particles were obtained, and images were processed with the EMAN2 software package. Shown is a gallery of class averages, with one representative particle from each class and the corresponding projection of the initial 3D reconstructions without symmetry applied (*Projection*^{1} columns) and with 432 symmetry applied (*Projection*^{2} columns). Particles, class averages, and projections representing the 2-, 3-, and 4-fold axis of the complex and intermediate orientations are shown sequentially from the *left* to the *right* starting with the *top row*. The particle diameter was 15.2 ± 0.8 nm (average of 103 particles with 2-fold orientations), 15.1 ± 0.7 nm (average of 123 particles with 3-fold orientations), and 15.4 ± 0.7 nm (average of 91 particles with 4-fold orientations). *B–G*, refined 3D models were generated without imposed symmetry (*B*) or with 432 symmetry applied (*E*). Both models were segmented using Chimera, and the 4-fold (*C* and *F*) and 3-fold (*D* and *G*) axes were identified and colored in *green* and *blue*, respectively. *H* and *I*, stereographic projection plots of the kappa = 90°(4-fold), kappa = 120° (3-fold), and kappa = 180° (2-fold) sections of the self-rotation function of the EM density map of the refined 3D model of the complex without symmetry applied (*H*) and with 432 symmetry applied (*I*), obtained using POLARRFN. *J* and *K*, PDBe Fourier shell correlation (*FSC*) server was used to calculate and plot the FSC curve for the refined 3D model without (*J*) and with 432 symmetry applied (*K*). The *dashed red line* shows where the FSC curve crosses the correlation value of 0.143.

obtained with the 3-σ criterion (13.7 and 15.5 Å) and the 1/2 bit criterion (16.0 and 14.9 Å) indicated that at these resolutions we had collected information significantly above the noise level and sufficient for interpretation (45).

We segmented the refined 3D models without and with 432 symmetry applied using Chimera (46), and we identified volumes with similar shapes around the 3- and 4-fold symmetry axes (Fig. 2, *C, D, F,* and *G*). Volumes around the 3-fold symmetry axes showed similar shape to the yeast $[\mathrm{Yfh1}]_3 \cdot [\mathrm{Isu1}]_3$ sub-complex, the building block of the $[\mathrm{Yfh1}]_{24} \cdot [\mathrm{Isu1}]_{24}$ complex (32). Based on this, FXN^{42-210} and ISCU trimers were modeled as described under "Experimental Procedures." Part of the extended N-terminal regions of FXN^{42-210} and ISCU (residues 42–93 and 36–50) were predicted to have a high degree of flexibility, and therefore N-terminally truncated trimers were created. We docked them into the segmented EM density map of the refined 3D model with 432 symmetry applied both separately (cross-correlation functions = 0.58 and 0.65, respectively) or together as a $[\mathrm{FXN}^{42-210}]_3 \cdot [\mathrm{ISCU}]_3$ sub-complex (cross-correlation function = 0.62), and we selected the latter mode of docking. Subsequently, nearby unoccupied densities were filled by modeling the N termini of FXN^{42-210} and ISCU using information obtained from chemical cross-linking (described in detail later). Nearby remaining segmented density of the 3D model revealed unoccupied volumes with similar shape to the homology model of the NFS1 monomer, which was docked into 24 similar volumes, with a cross-correlation coefficient of 0.57. After molecular dynamics simulations were completed (see below), we attempted docking of the simulated structures of the $[\mathrm{FXN}^{42-210}]_3 \cdot [\mathrm{ISCU}]_3$ sub-complex and NFS1 monomer into the segmented EM density map of the refined 3D model without symmetry applied. We were able to fit eight $[\mathrm{FXN}^{42-210}]_3 \cdot [\mathrm{ISCU}]_3$ sub-complexes (cross-correlation functions ranged from 0.37 to 0.54) and 24 NFS1 monomers (cross-correlation functions ranged from 0.41 to 0.56) (supplemental Fig. S1).

After fitting of FXN^{42-210}, ISCU, and NFS1 into the EM density map, cross-linking data and the presence of some unoccupied volumes just above the NFS1 subunits lead us to conclude that the ISD11 protein might be located on the surface of the complex. However, the unoccupied volumes at the surface of the refined 3D model were not sufficiently delineated from the background to enable docking of ISD11 monomers into the segmented EM map. Therefore, based on the measured NFS1: ISD11 stoichiometry of 1:1 and the cross-linking data, we modeled 24 ISD11 monomers on the surface of the 3D model with 432 symmetry applied but did not include ISD11 in the simulations described below.

Molecular Dynamics Flexible Fitting for Docked Structures—Attempts to simulate the entire docked structure of the complex (hereafter designated $[\mathrm{FXN}^{42-210}]_{24} \cdot [\mathrm{NFS1}]_{24} \cdot [\mathrm{ISD11}]_{24} \cdot [\mathrm{ISCU}]_{24}$) were unsuccessful due to the very large number of

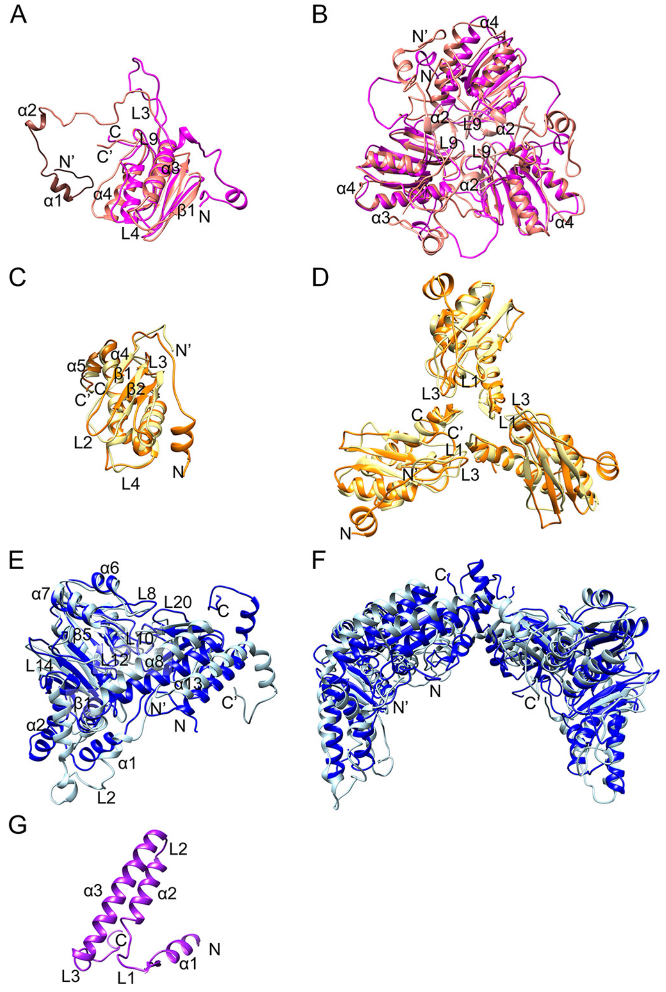

FIGURE 3. **Molecular dynamics flexible fitting for docked structures of FXN^{42-210}, NFS1, and ISCU proteins.** *A–F*, upon docking of eight $[\mathrm{FXN}^{42-210}]_3\cdot[\mathrm{ISCU}]_3$ sub-complexes and 24 NFS1 monomers into the EM density map of the refined 3D model with 432 symmetry applied, one-half of the docked structure was subjected to molecular dynamics simulations and energy minimizations as described under "Experimental Procedures." FXN^{42-210} monomer (*A*) and trimer (*B*) before (*magenta ribbon*; *N*, N terminus) and after (*salmon ribbon*; *N'*, N terminus); ISCU monomer (*C*) and trimer (*D*) before (*orange ribbon*; *N*, N terminus) and after (*yellow ribbon*; *N'*, N terminus); and NFS1 monomer (*E*) and dimer (*F*) before (*blue ribbon*; *N*, N terminus) and after (*light blue ribbon*; *N'*, N terminus) molecular dynamics simulations and energy minimizations. *G*, model of ISD11 monomer (*purple ribbon*; *N*, N terminus) obtained using the I-TASSER web resource, which was not included in the simulated structure as described under "Results."

atoms involved (>100,000). However, we were able to subject one-half of the structure, consisting of six NFS1 dimers docked on top of four $[\mathrm{FXN}^{42-210}]_3\cdot[\mathrm{ISCU}]_3$ sub-complexes, to mild simulation using Molecular Dynamics Flexible Fitting (47, 48) as described under "Experimental Procedures." Prior to the simulation, residues 42–98 in the N-terminal region of FXN^{42-210} were repositioned guided by cross-linking data. In addition, the N-terminal flexible portions of ISCU (residues 35–49) and NFS1 (residues 55–66) were removed to avoid steric clashes during the simulation. The simulation improved the fitting of the structure into the EM density map, as the cross-correlation coefficient improved from 0.46 to 0.62. After the simulation, the fold of the FXN^{42-210} monomer (Fig. 3*A*) and the overall arrangement of monomers in the FXN^{42-210} trimer (Fig. 3*B*) remained very similar to those in the docked structure, except for the N-terminal region (residues 42–93) that had been manually modeled into a different configuration based on cross-linking data (Fig. 3, *A* and *B*). The fold of the ISCU monomer (Fig. 3*C*) and the overall arrangement of monomers in the ISCU trimer (Fig. 3*D*) also matched the initial docked structure closely except for the absence of N-terminal residues 35–49 and for a small movement of loops L2, L3, and helix $\alpha5$ (Fig. 3, *C* and *D*). The fold of the NFS1 monomer (Fig. 3*E*) and the overall arrangement of the NFS1 dimer (Fig. 3*F*) remained very similar to those in the docked structure except for the following: (i) the absence of N-terminal residues 55–66; (ii) the C-terminal region that had been manually modeled into a different configuration based on cross-linking data; and (iii) a small movement of loop L2 and helices $\alpha1$, $\alpha2$, $\alpha8$, and $\alpha13$ (Fig. 3, *E* and *F*). As mentioned above, the modeled 24 ISD11 monomers (Fig. 3*G*) were not included in the simulation.

Overall Architecture of the Human Fe-S Cluster Assembly Complex—For the purpose of visualizing the entire complex structure, the simulated one-half was aligned with itself into the EM density map of the refined 3D model, followed by structure improvement iterations with the program Coot to resolve small steric clashes between NFS1 subunits at the interface between the two halves of the structure (Fig. 4, *A* and *F*). The complex consists of a central, roughly cubic $[\mathrm{FXN}^{42-210}]_{24}\cdot[\mathrm{ISCU}]_{24}$ sub-complex made up of one symmetric ISCU trimer bound on top of one symmetric FXN^{42-210} trimer at each of the eight vertices of the cube (Fig. 4, *A* and *C* and *F* and *H*), similar to the recently described yeast $[\mathrm{Yfh1}]_{24}\cdot[\mathrm{Isu1}]_{24}$ complex (32). In each $[\mathrm{FXN}^{42-210}]_3\cdot[\mathrm{ISCU}]_3$ sub-complex, there are three $[\mathrm{FXN}^{42-210}]\cdot[\mathrm{ISCU}]$ heterodimers in which one ISCU monomer is positioned on top of one FXN^{42-210} monomer with an approximate 5–10° rotation clockwise with respect to the FXN^{42-210} monomer's longitudinal axis (Fig. 4*C*). The monomers in each ISCU trimer form a channel at the 3-fold axis defined by the C terminus and loops L1 and L3 of each subunit (Figs. 3*D* and 4*C*) that is aligned with a similar channel at the 3-fold axis of the FXN^{42-210} trimer underneath, defined by loop L9 and helix $\alpha2$ of each subunit (Figs. 3*B* and 4*C*). Furthermore, 24 NFS1 monomers bind to the surface of the $[\mathrm{FXN}^{42-210}]_{24}\cdot[\mathrm{ISCU}]_{24}$ sub-complex forming a symmetric trimer and a symmetric tetramer at each of the 3- and 4-fold axes of the complex (Fig. 4, *A*, *B*, and *E* and *F*, *G*, and *J*). Binding of 24 NFS1 monomers results in a more spherical macromolecule (Fig. 4, *A* and *F*) as compared with the roughly cubic $[\mathrm{FXN}^{42-210}]_{24}\cdot[\mathrm{ISCU}]_{24}$ sub-complex (Fig. 4, *C* and *H*). Each 4-fold axis of the complex passes through the center of a pore delimited by four NFS1 subunits that rest on top of four $[\mathrm{FXN}^{42-210}]_3\cdot[\mathrm{ISCU}]_3$ sub-complexes (Fig. 4, *F–J*). Each 3-fold axis passes through the center of one $[\mathrm{FXN}^{42-210}]_3\cdot[\mathrm{ISCU}]_3$ sub-complex surrounded by one symmetric NFS1 trimer (Fig. 4, *A–E*). Each of the 12 2-fold axes of the complex passes through the center of one $[[\mathrm{FXN}^{42-210}]_3\cdot[\mathrm{ISCU}]_3]_2[\mathrm{NFS1}]_2$ sub-complex (Fig. 5, *A* and *B*), each comprising two of the 24 active centers of the complex (Fig. 5, *C* and *D*), as discussed later.

Cross-linking Analysis—We used chemical cross-linking and limited proteolysis of the complex, followed by MS/MS identification of cross-linked peptides as an independent means to

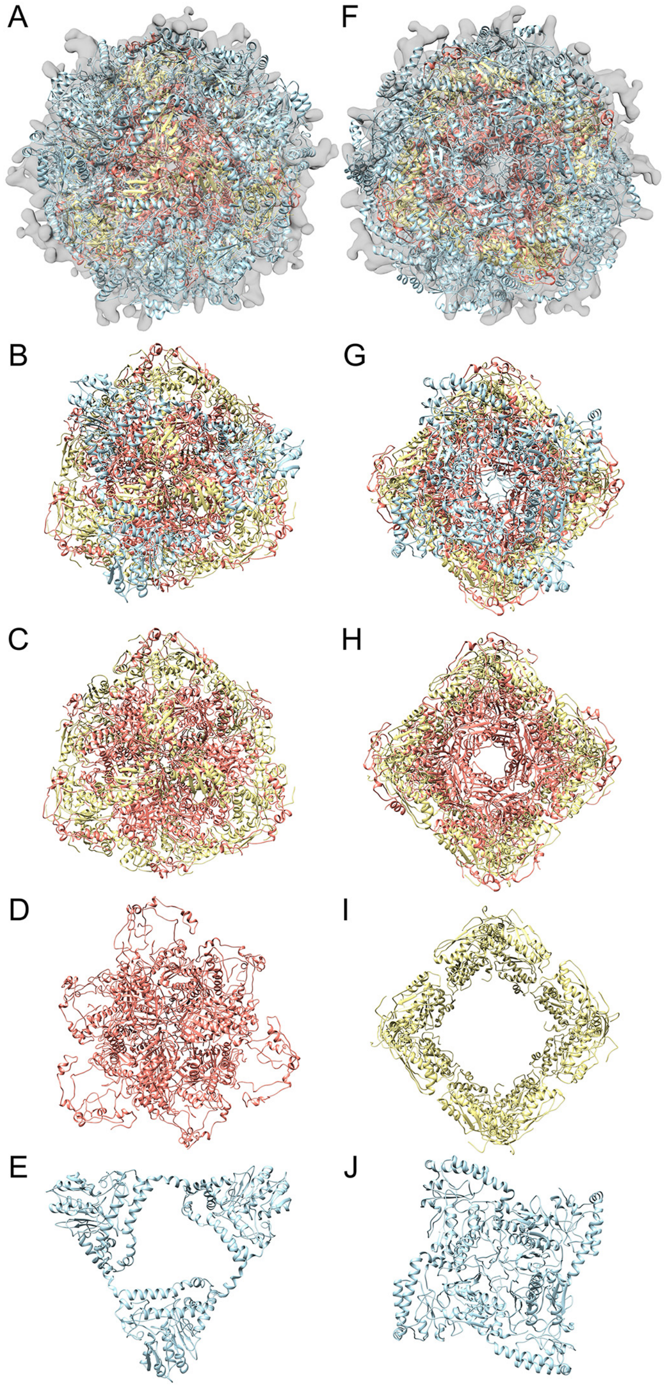

FIGURE 4. **Overall architecture of the human $[FXN^{42-210}]_{24}\cdot[ISCU]_{24}\cdot[NFS1]_{24}$ complex.** *A–F*, to visualize the structure of the entire complex, the simulated half of the structure was aligned with itself into the EM density map of the refined 3D model. The structure consists of 24 FXN^{42-210} (*salmon ribbon*), 24 ISCU (*yellow ribbon*), and 24 NFS1 (*light blue ribbon*) subunits. *A* and *F*, docked structure at the 3-fold (*A*) and 4-fold (*F*) axes of the complex. *B–J*, structural building blocks of the complex at the 3-fold axis (*B–E*) and the 4-fold axis (*G–J*) of the complex with EM density map removed.

obtain information about protein-protein interactions in the $[FXN^{42-210}]_{24}\cdot[ISCU]_{24}\cdot[NFS1]_{24}\cdot[ISD11]_{24}$ complex (49). Because the cross-linked complex was enzymatically active (Fig. 1*H*), it was suitable to obtain structural information. A summary of the results is presented in Table 2 and a detailed description in supplemental Table S2. Of the 124 cross-linked peptides identified, 43% had false discovery rate (FDR) ≤5% and 90% had FDR ≤25% (Table 2). The identified cross-links involved 13/13 Lys residues of FXN^{42-210} (Fig. 6*A*), 19/20 Lys residues of ISCU (Fig. 6*E*), 21/21 Lys residues of NFS1 (Fig. 7*A*), and 6/6 Lys residues of ISD11 (Fig. 7*F*). In addition, the identified cross-links involved the N-terminal amino groups and several Ser, Thr, and Tyr residues of FXN^{42-210}, ISCU, NFS1, or ISD11. Based on the general guidelines for this type of analysis (49), the large number of identified cross-links indicated a tight-binding four-protein complex.

Next, we assessed the degree of agreement between the structure of the complex and the cross-linking data by measuring, in the simulated half-structure of the complex, the distances between all possible pairs of cross-linked residues within any given cross-linked peptide (supplemental Table S2), by identifying mean distances (± S.D.) equal to or lower than the distance constraints or the maximum allowable distance constraints, or greater than the maximum allowable distance constraints (highlighted in light gray, dark gray, and yellow, respectively, in supplemental Table S2). Agreement between the simulated structure and any given cross-linked peptide was established if at least one of the mean distances measured in the simulated half-structure was within the distance constraints or the maximum allowable distance constraints (Table 2 and supplemental Table S2). When using the distance constraints, our simulated structure is in agreement with 80/124 or ~65% of the cross-linked peptides identified (Table 2). When using the maximum allowable distance constraints, the agreement increases to ~90% (Table 2). There is apparent disagreement between the simulated half-structure of the complex and 13/124 or ~10% of the cross-linked peptides identified (Table 2). These 13 peptides (denoted by asterisks in supplemental Table S2) involve flexible regions of the four proteins. Distances measured in the structure between cross-linked residues from 10 of the 13 peptides are only ~3–9 Å above the maximum allowable distance constraints, a difference that could be explained by the flexibility of the cross-linked regions.

Next, mapping of the cross-links in the simulated structure of the complex revealed that the cross-linking data support several recurring protein-protein interaction surfaces, including interfaces within individual FXN^{42-210}, ISCU, NFS1, or ISD11 subunits (Fig. 6, *B* and *F* and Fig. 7, *B* and *G*; supplemental Tables S2, *a–d*), between FXN^{42-210} or ISCU subunits of the same $[FXN^{42-210}]_3\cdot[ISCU]_3$ sub-complex (Fig. 6, *C* and *G*; supplemental Table S2, *a* and *b*), between FXN^{42-210} or ISCU subunits of two adjacent $[FXN^{42-210}]_3\cdot[ISCU]_3$ sub-complexes (Fig. 6, *D* and *H*; supplemental Table S2, *a* and *b*), and between NFS1 subunits of the same NFS1 dimer, trimer, or tetramer (Fig. 7, *C–E*; supplemental Table S2*c*). The symmetrical arrangement of the complex allows some FXN^{42-210}-FXN^{42-210} or ISCU-ISCU cross-links to be possible within the same monomer (supplemental Table S2, *a*, pp. 1–2, and *b*, pp. 1–8), between two monomers of the same trimer (supplemental Table S2, *a*, pp. 1–2, and *b*, pp. 1–8), or between monomers from two adjacent trimers (supplemental Table S2, *a*, pp. 1–2, and *b*, pp. 2, 3, and 7). For example, in the case of FXN^{42-210}, cross-links Thr-102–Lys-116, Ser-105–Lys-116, Tyr-123–Lys-135, Tyr-123–Lys-147, and Tyr-123–Lys-164 are possible within one FXN^{42-210}

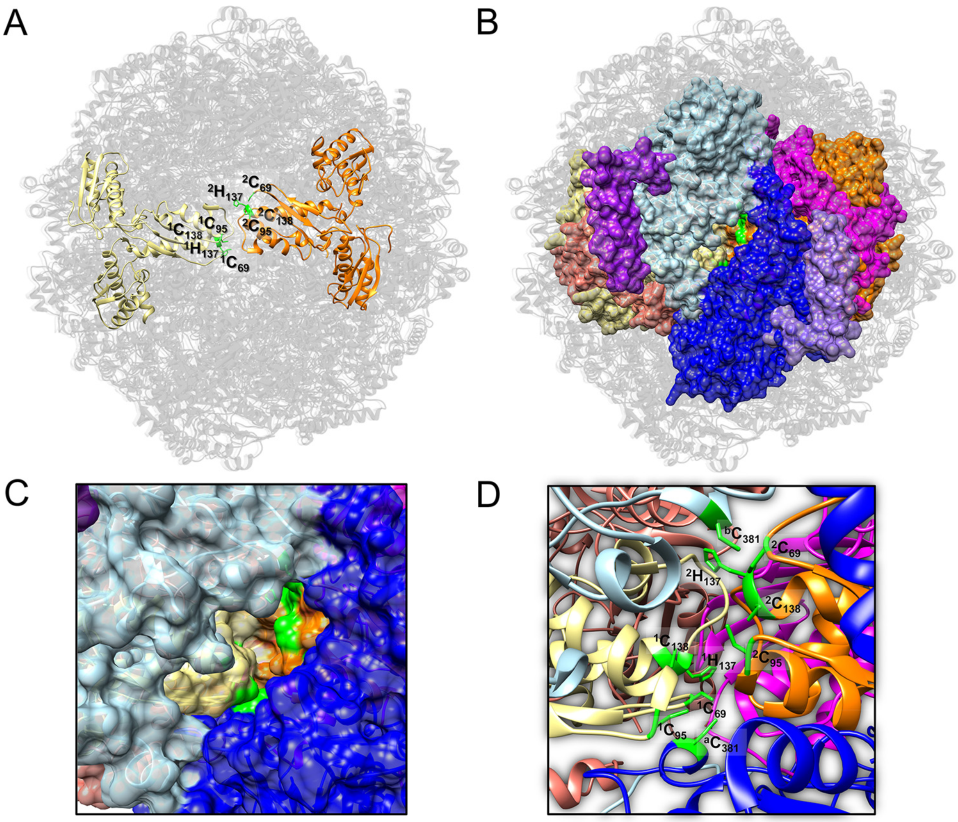

FIGURE 5. **Fe-S cluster assembly center at the 2-fold axis of the human $[FXN^{42-210}]_{24}\cdot[ISCU]_{24}\cdot[NFS1]_{24}$ complex.** *A*, top view of two Fe-S cluster assembly sites formed by two adjacent $[ISCU]_3$ sub-complexes at the 2-fold axis of the complex. ISCU trimers are shown as *yellow* and *orange ribbons* with Fe-S cluster coordinating residues shown as *green sticks*. The *numbers 1* and *2* denote the two adjacent ISCU trimers. *B*, as in *A* with addition of two adjacent FXN^{42-210} trimers shown as *salmon* and *magenta ribbons* and surfaces, and one $[NFS1]_2\cdot[ISD11]_2$ sub-complex, with NFS1 subunits shown as *light blue* and *blue ribbons* and surfaces, and ISD11 subunits shown as *purple* and *light purple ribbons* and surfaces. *C*, closer view of the two [2Fe-2S] assembly centers shown in *B*. *D*, same as *C* but with surfaces removed. The *numbers 1* and *2* denote the two adjacent ISCU trimers, and the *letters a* and *b* the two adjacent NFS1 monomers. The structure of the $[FXN^{42-210}]_6\cdot[NFS1]_2\cdot[ISCU]_6$ sub-complex was extracted from the simulated half-structure of the complex, whereas ISD11 subunits were modeled at the surface of the complex as described under "Results."

subunit (Fig. 6*B*) or between subunits of two adjacent trimers (Fig. 6*D*). Similarly, cross-links Lys-135–Lys-152 and Lys-135–Lys-164 are possible within one FXN^{42-210} subunit (Fig. 6*B*) or between subunits of two adjacent trimers (Fig. 6*D*); although based on distances measured in the simulated structure, these particular cross-links are more likely to form between subunits of two adjacent FXN^{42-210} trimers (supplemental Table S2*a*, pp. 1 and 2). Similarly, in the case of ISCU, cross-link Lys-127–Lys 135, which is part of the highly conserved PVK (Pro-133, Val-134, and Lys-135) motif of ISCU (50), is possible both within the same ISCU subunit (Fig. 6*F*) and between ISCU subunits of two adjacent ISCU trimers (Fig. 6*H*; supplemental Table S2*b*, p. 3). However, cross-links Lys-160–Lys-160 and Lys-161–Lys-161 are only possible between two adjacent ISCU subunits of the same trimer (Fig. 6*G*; supplemental Table S2*b*, p. 2). Most of the NFS1-NFS1 cross-links could only form within the same NFS1 monomer (Fig. 7*B*; supplemental Table S2*c*, pp. 1–4). However, certain cross-links could only be explained by the presence of adjacent NFS1 subunits. In particular, the Lys-157–Ser-437 cross-link could only be possible in the context of the NFS1 dimer at the 2-fold axis of the complex (Fig. 7*C*; supplemental Table S2*c*, p. 1); the Ser-437–Lys-320 cross-link in the context of the NFS1 trimer at the 3-fold axis of the complex (Fig. 7*D*; supplemental Table S2*c*, p. 1); and the Ser-99–Lys-157 cross-link in the context of NFS1 tetramer at the 4-fold axis of the complex (Fig. 7*E*; supplemental Table S2*c*, p. 2). ISD11-ISD11 cross-links support the fold of the modeled ISD11 monomer (Fig. 7*G*; supplemental Table S2*d*, p. 1).

At the 2-fold axis of the complex, which is formed by one symmetric $[NFS1]_2\cdot[ISD11]_2$ heterodimer resting on top of two adjacent $[FXN^{42-210}]_3\cdot[ISCU]_3$ sub-complexes (Figs. 5*B* and 8*A*), the cross-links are in good agreement with the following protein-protein interaction surfaces as follows: between FXN^{42-210} and ISCU subunits of the same $[FXN^{42-210}]\cdot[ISCU]$ heterodimer (Fig. 9*A*); between FXN^{42-210} and ISCU subunits of the same $[FXN^{42-210}]_3\cdot[ISCU]_3$ sub-complex (Fig. 9*B*); between FXN^{42-210} and ISCU subunits of two adjacent $[FXN^{42-210}]_3\cdot[ISCU]_3$ sub-complexes (Fig. 9*C*); between each of the two NFS1 subunits and (i) two FXN^{42-210} subunits of the same FXN^{42-210} trimer and one FXN^{42-210} subunit from the adjacent trimer (Fig. 9*D*), and (ii) one ISCU subunit from each of the two adjacent ISCU trimers (Fig. 9*E*). Based on actual mean distances measured between all possible pairs of cross-linked residues, some cross-links are possible within one $[FXN^{42-210}]\cdot[ISCU]$ heterodimer (Fig. 9*A*; supplemental Table S2*e*, pp. 1–3) and also between two heterodimers within the same $[FXN^{42-210}]_3\cdot[ISCU]_3$ sub-complex (Fig. 9*B*; supplemental Table S2*e*, pp. 1–3) and between two adjacent sub-com-

TABLE 2
Summary of cross-linking results

Cross-linked peptides were identified, and the distance constraints and maximum allowable distance constraints between different pairs of cross-linked residues were calculated as described under "Experimental Procedures." Agreement between the simulated three-dimensional structure and any given cross-linked peptide was established as described under "Results." The data summarized in this table are shown in detail in supplemental Table S2.

Cross-linked partners	Total cross-linked peptides	FDR ≤5 (%)	FDR ≤10 (%)	FDR ≤15 (%)	FDR ≤20 (%)	FDR ≤25 (%)	FDR ≤35 (%)	FDR ≤45 (%)	FDR ≤60 (%)	Cross-linked peptides that support complex structure based on distance constraints	Cross-linked peptides that support complex structure based on maximum allowable distance constraints	Cross-linked peptides in disagreement with complex structure
		%	%	%	%	%	%	%	%			
FXN^{42-210}-FXN	6	2				3		1		5	1	
FXN^{42-210}-ISCU	13	4			4	1	1	1	2	10	3	
FXN^{42-210}-ISD11	4	2				1		1		1		3
FXN^{42-210}-NFS1	12	3	1		4	2		1	1	4	7	1
ISCU-ISCU	26	16	3	1	3	3				26		
ISCU-ISD11	4					1	2		1	2	1	1
ISCU-NFS1	22	10	2		8	2				9	8	5
ISD11-ISD11	4	2				1	1			2	2	
ISD11-NFS1	11	3			5	3				6	4	1
NFS1-NFS1	22	11	3		6	1	1			15	5	2
Total	124	53	9	1	30	18	5	4	4	80	31	13
% of total	100%	43%	7%	1%	24%	15%	4%	3%	3%	65%	25%	10%

plexes (Fig. 9*C*; supplemental Table S2*e*, pp. 1–3). In contrast, FXN^{42-210}-ISCU cross-links Tyr-95–Lys-160 (or Lys-161) and Lys-135–Lys-160 (or Lys-167) are only possible in the latter two instances (Fig. 9, *B* and *C*; supplemental Table S2*e*, pp. 1 and 3). Interestingly, Lys-135 of ISCU (part of the highly conserved PVK motif) forms a cross-link with Tyr-175, located on loop L9 of FXN^{42-210} (Fig. 9*C*; supplemental Table S2*e*, p. 2), and with Ser-404 and/or Ser-405, located on helix α12 of NFS1 (Fig. 9*E*; supplemental Table S2*g*, p. 4), close to the active center Cys-381 (shown later in Fig. 14*F*). Some ISCU-NFS1 cross-links are made possible by the trimeric arrangement of ISCU subunits, which creates different interfaces with NFS1, for example helix α1 (Lys-110 and/or Lys-112) of ISCU and helix α13 (Tyr-421 and/or Thr-422) of NFS1; the C-terminal portion of ISCU (Lys-166 and/or Lys-167) and helix α2 (Ser-99) of NFS1; helix α4 (Lys-147) of ISCU and helix α11 (Ser-383 and/or Ser-385) of NFS1 (Fig. 9*E*; supplemental Table S2*g*, pp. 2 and 3). In addition, the cross-links support protein-protein interactions between each ISD11 subunit and both the NFS1 subunit and the $[FXN^{42-210}]\cdot[ISCU]$ heterodimer underneath (Figs. 8*A* and 9*G*). A large number of ISD11-NFS1 cross-linked peptides identified support the position of one ISD11 subunit along helices α8 and α13 of each NFS1 subunit (Figs. 8, *A–C*, and 9*G*). There are four ISD11-FXN^{42-210} cross-links (between (i) helix α2 (Lys-44 and/or Lys-47) of ISD11 and the N-terminal region (Lys-69 and/or Lys-70) of FXN^{42-210}; (ii) helix α2 (Lys-44 and/or Lys-47) of ISD11 and the C-terminal region (Lys-197) of FXN^{42-210}; (iii) the N terminus of ISD11 (N-term) and helix α3 (Ser-105) of FXN^{42-210} (Fig. 9*G*); and (iv) helix α2 (Lys-44 and/or Lys-47) of ISD11 and loop L3 (Thr-93 and/or Tyr-95) of FXN^{42-210} (only i–iii are shown in Fig. 9*G*). There are also four ISD11-ISCU cross-links (between (i) the C-terminal regions of both proteins (Thr-91 of ISD11 and Lys-161 of ISCU); (ii) the N terminus of ISD11 and helix α3-loop L7 (Lys-121 and/or Lys-127) of ISCU; (iii) the N terminus of ISD11 and the C-terminal region (Lys-160 and/or Lys-161) of ISCU; and (iv) helix α2 and loop L2 (Lys-44 and/or Lys-47) of ISD11 and helix α4 (Lys-147 and/or Lys-156) of ISCU (Fig. 9*G*)). These cross-links support the position of each ISD11 subunit relative to the $[FXN^{42-210}]\cdot[ISCU]$ heterodimer underneath (Fig. 9*G*).

At the 3-fold axis of the complex, which is formed by one $[FXN^{42-210}]_3\cdot[ISCU]_3$ sub-complex surrounded by one symmetric $[NFS1]_2\cdot[ISD11]_2$ heterotrimer and by three more peripheral $[NFS1]\cdot[ISD11]$ heterodimers (Fig. 8*B*), the cross-links support the same protein-protein interaction surfaces described above as well as protein-protein interactions, not present in the 2-fold axis, between each of the three peripheral $[NFS1]\cdot[ISD11]$ heterodimers with FXN^{42-210} and ISCU subunits from adjacent $[FXN^{42-210}]\cdot[ISCU]$ heterodimers (Figs. 8*B* and 9*F*). Finally, at the 4-fold axis of the complex, which is formed by one symmetric $[NFS1]_2\cdot[ISD11]_2$ heterotetramer resting on top of four $[FXN^{42-210}]_3\cdot[ISCU]_3$ subcomplexes, the cross-links once again support the same protein-protein interaction surfaces described above (Figs. 8*C* and 9, *A–E* and *G*).

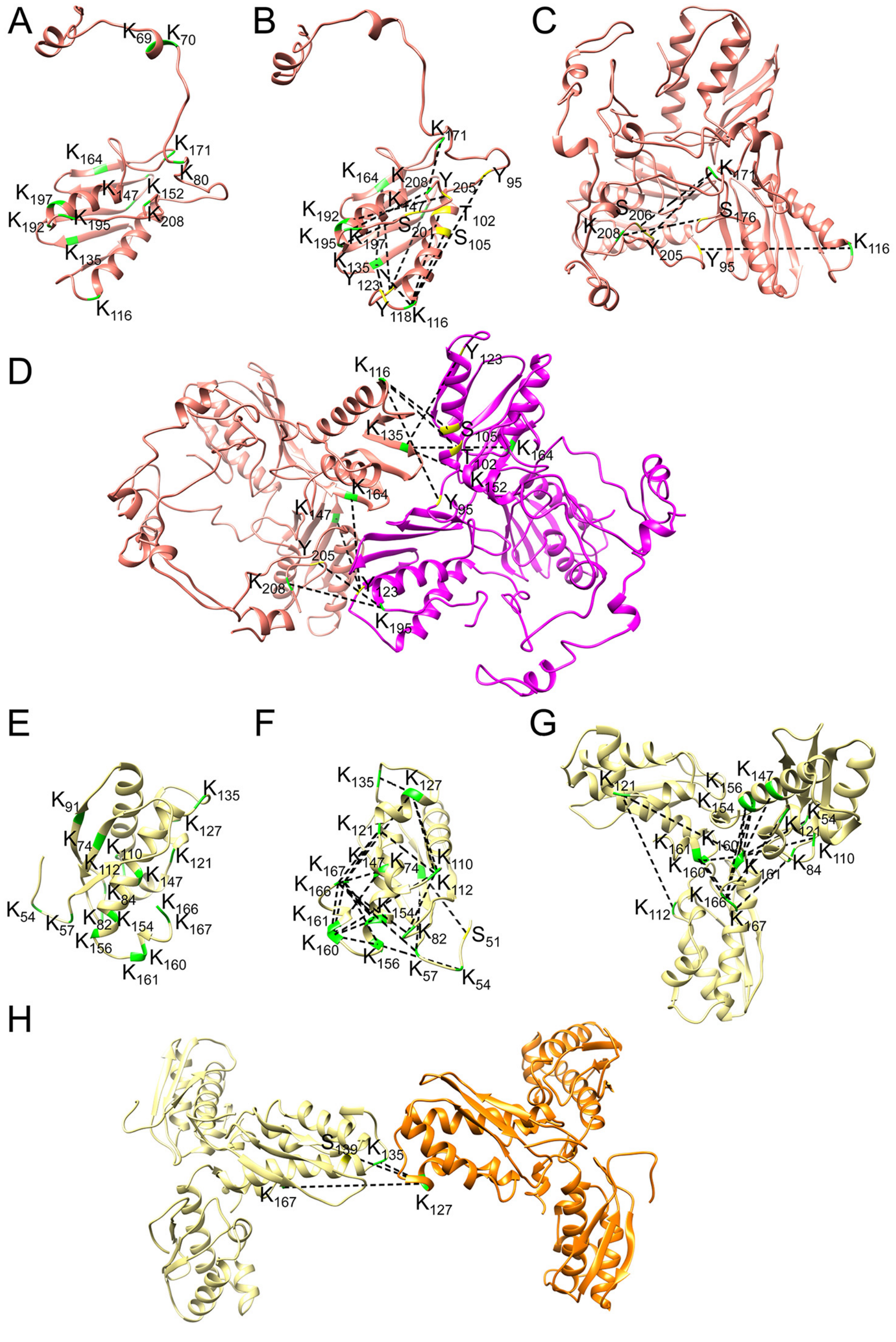

FIGURE 6. **Architecture of FXN$^{42–210}$ and ISCU trimers analyzed using chemical cross-linking.** *A* and *E*, Lys residues (*K*, shown in *green*) available for cross-linking with BS^3 in each FXN$^{42–210}$ (*A*) and ISCU (*E*) monomer. *B–D* and *F–H*, mapping of representative cross-links (*dotted lines*; Lys residues are in *green* and non-Lys residues in *yellow*) in the simulated structures of FXN$^{42–210}$ and ISCU monomers and trimers (see supplemental Table S2, *a* and *b*, for a detailed analysis of all cross-links identified). *B*, FXN$^{42–210}$ subunit structure fulfills the distance constraints set by cross-links *K192–Y205, K195–S201, K197–K208, K171–K208, K116–S105, K116–K135, Y118–K135, Y123–K147,* and *Y123–K164*, and the maximum allowable distance constraints set by cross-links *K116–Y95* and *K116–T102* (supplemental Table S2*a*, pp. 1 and 2). *C*, FXN$^{42–210}$ trimer structure fulfills the distance constraints set by cross-link *K171–Y205*, and the maximum allowable distance constraints set by cross-links *K208–S176, K171–S206,* and *K116–Y95* (supplemental Table S2*a*, p. 1). *D*, structure of two adjacent FXN$^{42–210}$ trimers fulfills the distance constraints set by cross-links *K135–K152, K135–K164, K116–S105, Y123–K135, Y123–K147,* and *Y123–K164*, and the maximum allowable distance constraints set by cross-links *K195–Y205, K195–K208, K116–Y95,* and *K116–T102* (supplemental Table S2*a*, pp. 1 and 2). *F*, ISCU subunit structure fulfills the distance constraints set by cross-links *S51–K74, K54–K156, K57–K74, K57–K166, K82–K112, K110–K127, K112–K121, K112–K127, K121–K166, K127–K135, K127–K167, K147–K160, K147–K166, K154–K160, K154–K166, K154–K167, K156–K160, K156–K167, K160–K167, K161–K166, K112–K160,* and *K82–K166* (supplemental Table S2*b*, pp. 1–4 and 7). *G*, ISCU trimer structure fulfills the distance constraints set by cross-links *K54–K160, K121–K160, K147–K160, K154–K161, K154–K166, K156–K160, K156–K166, K160–K167, K161–K166, K110–K160, K160–K160,* and *K84–K167*, and the maximum allowable distance constraints set by cross-links *K112–K121* and *K121–K166* (supplemental Table S2*b*, pp. 1, 2, 4, and 7). *H*, structure of two adjacent ISCU trimers fulfills the distance constraints set by cross-links *K127–K135* and *K127–S139*, and the maximum allowable distance constraints set by cross-link *K127–K167* (supplemental Table S2*b*, pp. 2, 3, and 7).

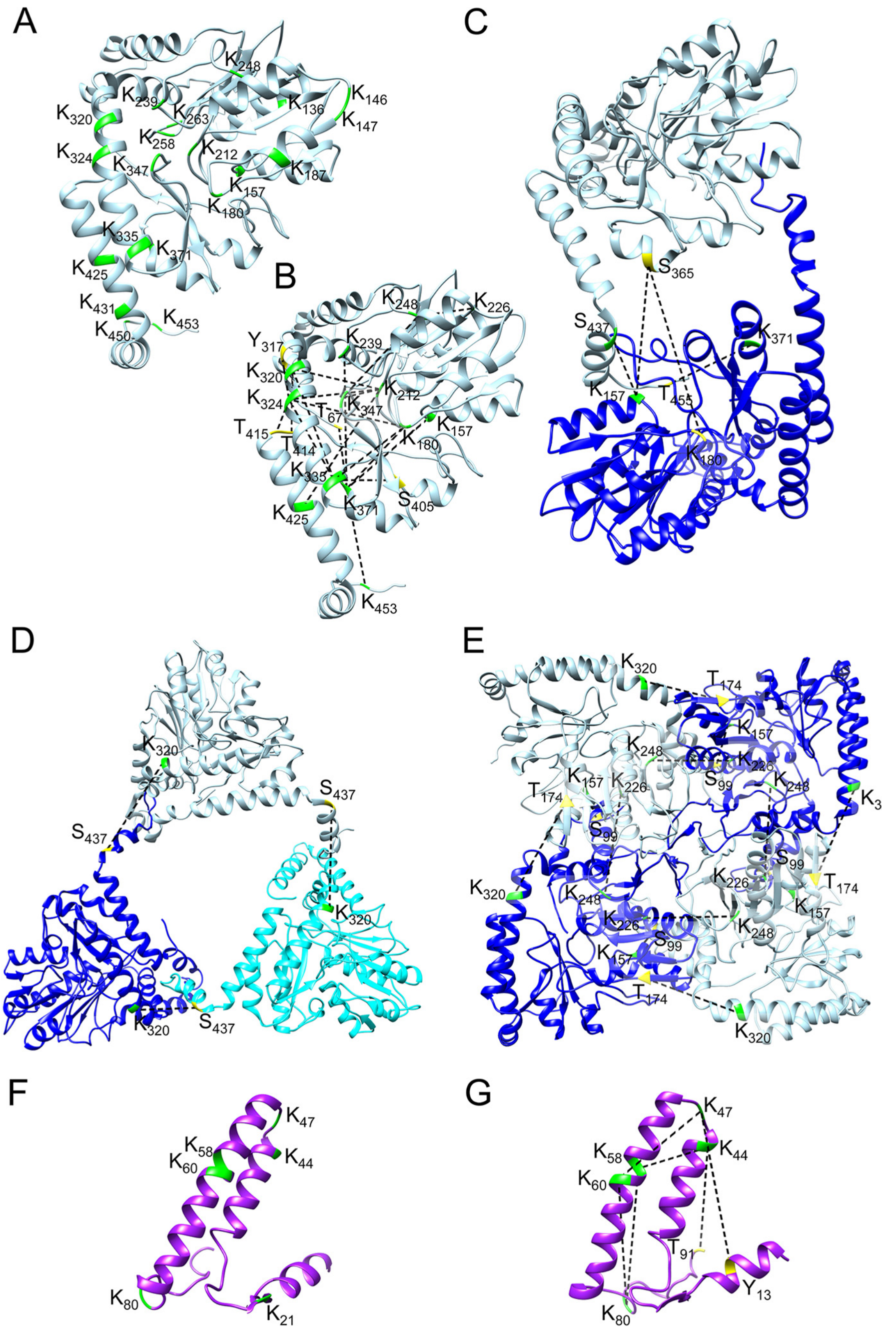

FIGURE 7. **Architecture of NFS1 monomer, dimer, trimer, and tetramer and of ISD11 monomer analyzed using chemical cross-linking.** *A* and *F*, Lys residues (*K*, shown in *green*) available for cross-linking with BS^3 in each NFS1 (*A*) and ISD11 (*F*) monomer. *B–E* and *G*, mapping of representative cross-links (*dotted lines*; Lys residues are in *green* and non-Lys residues in *yellow*) in the simulated structures of NFS1 monomer, dimer, trimer, and tetramer, and the modeled ISD11 monomer (see supplemental Table S2, *c* and *d* for a detailed analysis of all cross-links identified). *B*, NFS1 subunit structure fulfills the distance constraints set by cross-links *K180–K324, K180–K335, K212–K320, K212–K324, K226–K248, K239–K371, K248–K347, K320–K335, K324–K335, K180–K371, K324–Y317, K157–K371, K320–T414, K324–T415*, and *K335–S405* and the maximum allowable distance constraints set by cross-links *K371–K453* and *K212–K425* (supplemental Table S2*c*, pp. 1–4). *C*, NFS1 dimer structure fulfills the distance constraints set by cross-link *K157–S437*, and the maximum allowable distance constraints set by cross-links *K371–T455, K180–S365*, and *K157–S365* (supplemental Table S2*c*, pp. 1, 3, and 4). *D*, NFS1 trimer structure fulfills the distance constraints set by cross-link *K320–S437* (supplemental Table S2*c*, p. 1). *E*, NFS1 tetramer structure fulfills the distance constraints set by cross-links *K157–S99* and *K226–K248*, and the maximum allowable distance constraint set by cross-link *K320–T174* (supplemental Table S2*c*, pp. 2 and 3). *G*, ISD11 subunit structure fulfills the distance constraints set by cross-links *K44–Y13, K44–K58*, and *K47–K60*, and the maximum allowable distance constraints set by cross-links *K47–Y13, K58–K80, K60–K80*, and *K44-T91* (supplemental Table S2*d*, p. 1).

Contact Surfaces of $[FXN^{42-210}]_{24}$*·*$[NFS1]_{24}$*·*$[ISCU]_{24}$ *Sub-complex*—We used the program PISA (51) to identify all possible interfaces between the FXN^{42-210}, ISCU, and NFS1 protein chains in the 2-fold axis of the simulated structure of the complex, formed by one symmetric $[NFS1]_2$ dimer resting on top of two adjacent $[FXN^{42-210}]_3$·$[ISCU]_3$ sub-complexes (Fig. 5*B*). The program identified 12 main interfaces (two FXN^{42-210}-FXN^{42-210}; one NFS1-NFS1; two ISCU-ISCU; two NFS1-FXN^{42-210}; two NFS1-ISCU; and three FXN^{42-210}-ISCU interfaces), including nine recurring interfaces and three

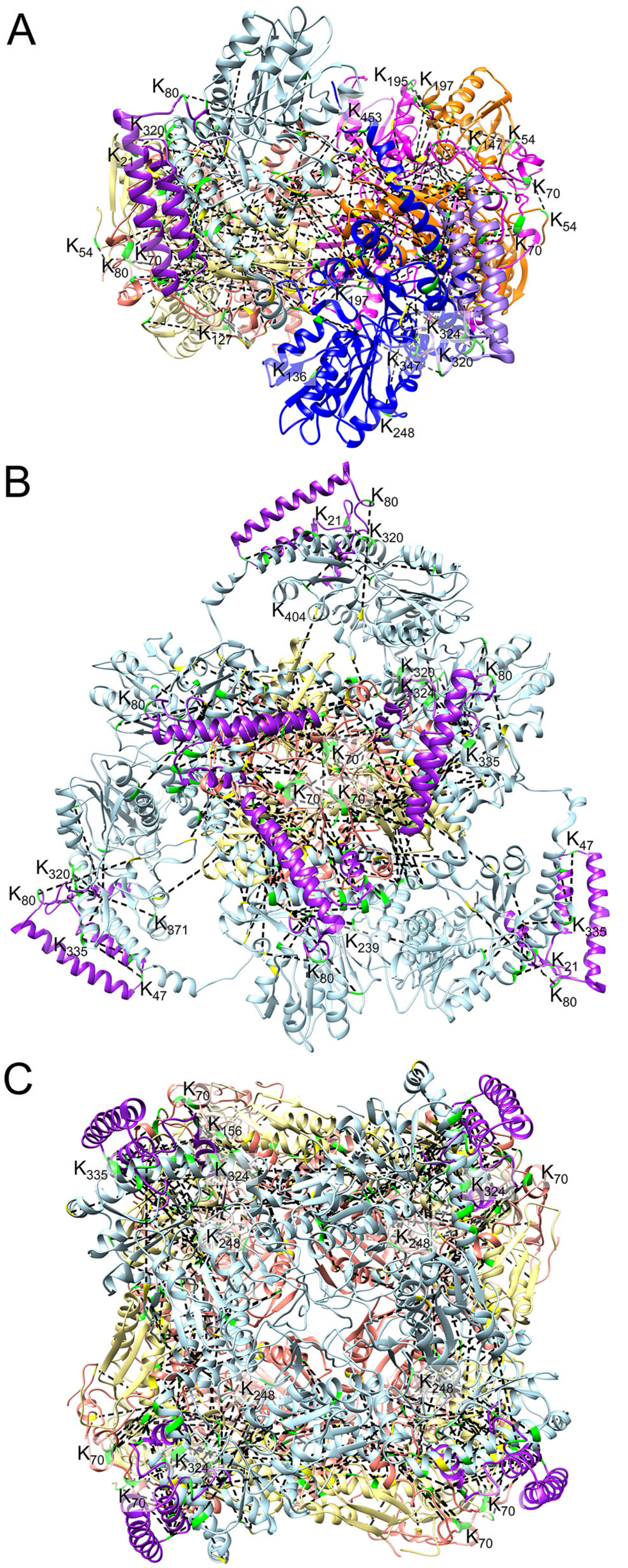

FIGURE 8. **Architecture of the $[FXN^{42-210}]_{24}$·$[ISCU]_{24}$·$[NFS1]_{24}$·$[ISD11]_{24}$ complex analyzed using primary amine-specific cross-linking.** *A–C*, mapping of representative FXN^{42-210}-ISCU, FXN^{42-210}-NFS1, FXN^{42-210}-ISD11, NFS1-ISCU, and NFS1-ISD11 cross-links (*dotted lines*; Lys residues are in *green* and non-Lys residues in *yellow*) at the 2-fold axis (90 recurring cross-links are shown) (*A*), 3-fold axis (85 recurring cross-links are shown) (*B*), and 4-fold axis (85 recurring cross-links are shown) (*C*) of $[FXN^{42-210}]_{24}$·$[ISCU]_{24}$·$[NFS1]_{24}$·$[ISD11]_{24}$ complex. Most cross-links are shown in detail in Fig. 9.

unique interfaces with buried surface area (BSA) of >300 Å^2 (Figs. 10–12), and four additional minor interfaces with BSA of ≤ 150 Å^2 (data not shown).

FXN^{42-210}-ISCU contacts include three main interfaces with BSA of ~1646 Å^2 (average of six recurring interfaces), 682 Å^2 (average of six recurring interfaces), and 331 Å^2 (unique interface). About 30 residues of ISCU and 30 residues of FXN^{42-210} are present in the largest interface of ~1646 Å^2 within the $[FXN^{42-210}]$·[ISCU] heterodimer, 23 of which are invariant in eukaryotes and 20 are invariant in mammals (Fig. 10*A*; supplemental Table S3). The FXN^{42-210} N terminus and several residues from the N terminus as well as the β-sheet of ISCU together contribute to this interface. Residues in the C terminus of FXN^{42-210} and two flexible α-helices, $\alpha 2$ and $\alpha 3$, of ISCU also contribute to this interface (Fig. 10*A*). All residues shown in Fig. 10*A* are predicted to form hydrogen bonds between the two proteins. In addition, several conserved residues are involved in salt bridges between ISCU and FXN^{42-210} (supplemental Table S3). Charge analysis of this interface in the context of the entire $[FXN^{42-210}]_3$·$[ISCU]_3$ sub-complex shows that the ISCU trimer surface is mostly positively charged, whereas the FXN^{42-210} trimer surface is mostly negatively charged, suggesting that electrostatic interactions may contribute to formation and stability of the sub-complex (Fig. 10, *B–D* and *C–E*). Another interface is present between one FXN^{42-210} subunit and one adjacent ISCU subunit within the same $[FXN^{42-210}]_3$·$[ISCU]_3$ sub-complex with BSA of ~682 Å^2 (Fig. 11*A*; supplemental Table S3). The FXN^{42-210} N-terminal flexible loop L3 and several residues from C-terminal helices $\alpha 4$ and $\alpha 5$ of ISCU contribute to this interface. Several conserved residues are predicted to form salt bridges between ISCU and FXN^{42-210}. These two interfaces show the important role of the FXN^{42-210} N terminus in stabilizing FXN^{42-210}-ISCU interactions within the same $[FXN^{42-210}]_3$·$[ISCU]_3$ sub-complex. In the third interface with BSA of ~331 Å^2, FXN^{42-210} residues from loops L6 and L10 interact with one subunit of ISCU from an adjacent $[FXN^{42-210}]_3$·$[ISCU]_3$ sub-complex (Fig. 11*B*; supplemental Table S3). In addition, residues in and around the PVK motif (shown as a *red ribbon*) of one ISCU subunit are involved in hydrophobic interactions with one FXN^{42-210} subunit from the adjacent $[FXN^{42-210}]_3$·$[ISCU]_3$ sub-complex (Fig. 11*G*).

There are two ISCU-ISCU interfaces with BSA of ~412 Å^2 (average of six recurring interfaces) and 298 Å^2 (unique interface), respectively. The first is formed by three ISCU subunits of the same trimer around the 3-fold axis, involving hydrogen bonds between the highly conserved Glu-81 and Gly-83 residues, and salt bridges between residues in the C terminus of each subunit, which are invariant in mammals (Fig. 11, *C* and *H*; supplemental Table S3). The second ISCU-ISCU interface is formed between two ISCU subunits of adjacent ISCU trimers via interactions between residues Cys-69–Cys-130, where Cys-69 is part of the highly conserved Fe-S cluster coordination site of ISCU (Fig. 11*D*). Additionally, this interface involves hydrophobic residues in and around the PVK motifs of two ISCU subunits from adjacent $[FXN^{42-210}]_3$·$[ISCU]_3$ sub-complexes (Fig. 11*I*).

There are two FXN^{42-210}-FXN^{42-210} interfaces with BSA of ~1150 and 304 Å^2 (average of six and two recurring interfaces,

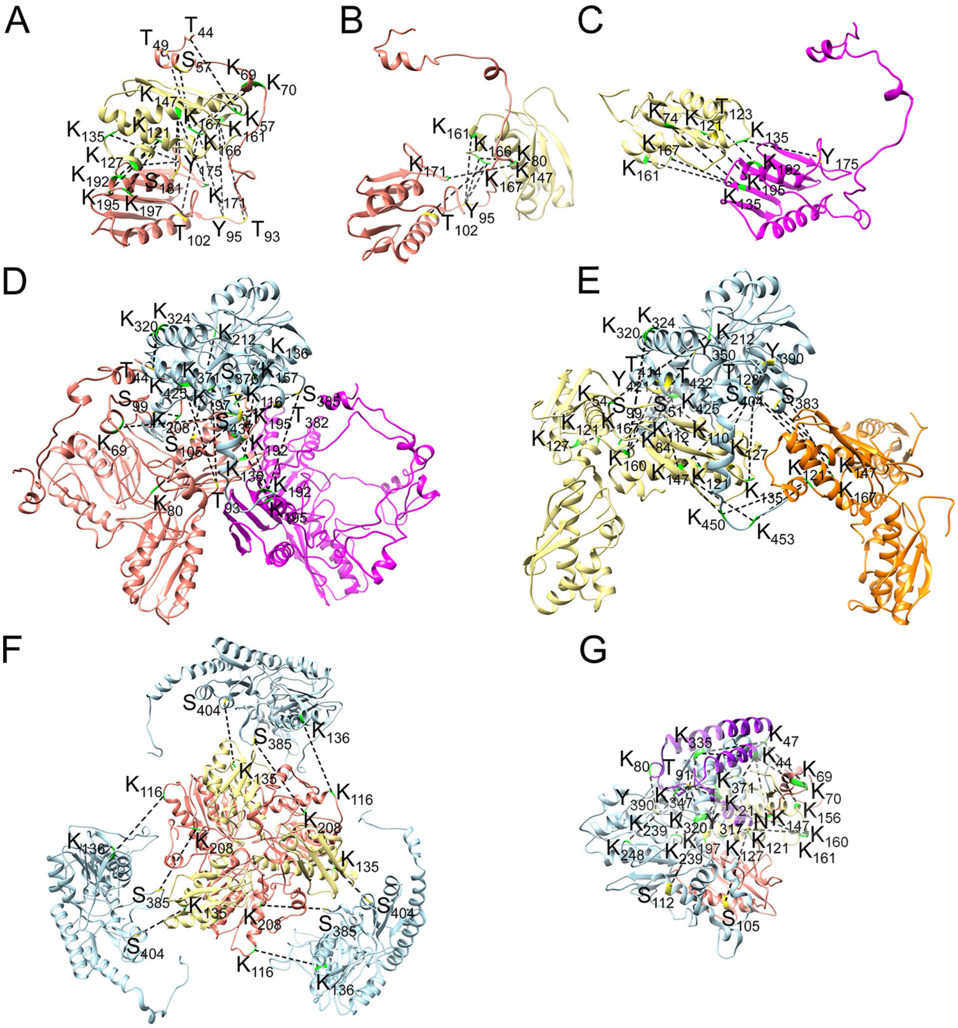

FIGURE 9. **Architecture of the [FXN$^{42-210}$]·[ISCU], [FXN$^{42-210}$]·[NFS1], [ISCU]·[NFS1], and [FXN$^{42-210}$]·[ISCU]·[NFS1]·[ISD11] sub-complexes analyzed using primary amine-specific cross-linking.** *A*, [FXN$^{42-210}$]·[ISCU] heterodimer structure fulfills the distance constraints set by FXN$^{42-210}$-ISCU cross-links *T49–K167, S57–K167, K69–K166, K171–K147, Y175–K127, Y175–K135, Y175–K147, S181–K147, K192–K121, K195–K121,* and *K197–K121*, and the maximum allowable distance constraints set by cross-links *T93–K161, Y95–K161, T102–K166, Y95–K166,* and *K70–K167* (supplemental Table S2*e*, pp. 1–3). *B*, arrangement of adjacent FXN$^{42-210}$ and ISCU subunits within the same [FXN$^{42-210}$]$_3$·[ISCU]$_3$ sub-complex fulfills the distance constraints set by FXN$^{42-210}$-ISCU cross-links *K80–K166, Y95–K161, T102–K167, K171–K147, Y95–K166,* and *Y95–K167* (supplemental Table S2*e*, pp. 1–3). *C*, arrangement of FXN$^{42-210}$ and ISCU subunits from two adjacent [FXN$^{42-210}$]$_3$·[ISCU]$_3$ sub-complexes fulfills the distance constraints set by FXN$^{42-210}$-ISCU cross-links *Y175–K135, K192–T123, K195–K121,* and *K135–K167*, and the maximum allowable distance constraints set by cross-links *K135–K74* and *K135–K161* (supplemental Table S2*e*, pp. 1–3). *D*, at the 2-fold axis of the complex, the arrangement of each subunit of the NFS1 dimer relative to FXN$^{42-210}$ subunits from two adjacent FXN$^{42-210}$ trimers fulfills the distance constraints set by FXN$^{42-210}$-NFS1 cross-links *T44–K320, K192–K371, K195–K371, K197–K371, K192–S385, K195–S385, K197–T382, K208–S99, K116–K136,* and *K116–K157*, and the maximum allowable distance constraint set by cross-links *T93–K425, T93–K371, K135–K157, K69–S437,* and *K80–S437* (supplemental Table S2*f*, pp. 1–3); the structure exceeds by ~9 Å the maximum allowable distance constraint set by cross-link *S105–K212* (supplemental Table S2*f*, p. 1). *E*, at the 2-fold axis of the complex, the arrangement of each subunit of the NFS1 dimer relative to ISCU subunits from two adjacent ISCU trimers fulfills the distance constraints set by ISCU-NFS1 cross-links *S51–K425, K110–T422, K112–Y421, K147–S383, K147–K450, K147–K453, K84–Y350, K127–S99, K135–S404,* and *K160–Y421* and the maximum allowable distance constraints set by cross-links *K121–K450, K121–K453, K160–K320, K160–K324, K167–Y390, K121–Y421, K127–Y421, K147–S404, K147-T414, K160–K425, K167–S99,* and *K127–Y390* (supplemental Table S2*g*, pp. 1–5); the structure exceeds by 2–6 Å the maximum allowable distance constraints set by cross-links *K167–T128, K147–T128,* and *K54–K212* (supplemental Table S2*g*, pp. 1, 2, and 4). *F*, at the 3-fold axis of the complex, the arrangement of NFS1 subunits relative to FXN$^{42-210}$ and ISCU subunits of one [FXN$^{42-210}$]$_3$·[ISCU]$_3$ sub-complex fulfills the distance constraints set by ISCU-NFS1 cross-link *K135–S404* (supplemental Table S2*g*, p. 4), and the maximum allowable distance constraints set by FXN$^{42-210}$-NFS1 cross-links *K208–S385* and *K116–K136* (supplemental Table S2*f*, pp. 1 and 2). *G*, the arrangement of the [NFS1]·[ISD11] heterodimer relative to the [FXN$^{42-210}$]·[ISCU] heterodimer underneath fulfills (i) the distance constraints set by FXN$^{42-210}$-ISD11 cross-links *K69–K44* and *K70–K47* (supplemental Table S2*h*, p. 2) [it exceeds by ~1–4 Å the maximum allowable distance constraints set by cross-links *K197–K44* and *S105–N-term* (supplemental Table S2*h*, p. 1)]; (ii) the distance constraints set by ISCU-ISD11 cross-links *K147–K44, K156–K47,* and *K160–N-term*, and the maximum allowable distance constraints set by cross-links *K121–N-term* and *K127–N-term* (supplemental Table S2*h*, pp. 3 and 4) [it exceeds by ~7 Å the maximum allowable distance constraints set by cross-link *K161–T91* (supplemental Table S2*h*, p. 3)]; (iii) the distance constraints set by NFS1-ISD11 cross-links *K335–K44, K335–K47, Y317–K21, K347–T91, K371–T91, K320–T91, K335–T91,* and *K239–T91*, and the maximum allowable distance constraints set by cross-links *Y390-K80* and *K248-T91* [it exceeds by ~3 Å the maximum allowable distance constraints set by cross-link *S112–K21* (supplemental Table S2*h*, pp. 5 and 6)].

respectively). The first is formed by FXN$^{42-210}$ subunits of the same trimer around the 3-fold axis and involves ~40 residues, 25 of which are conserved in eukaryotes (Fig. 11*E*). PISA-identified salt bridges involve residues in the N-terminal region of one subunit and residues in loop L3, helix α3, loop L9, and the C terminus of another subunit. PISA-identified hydrogen bonds involve residues between the N-terminal region, loop L3, and helix α3 of one subunit and loops L8 and L9 of another subunit,

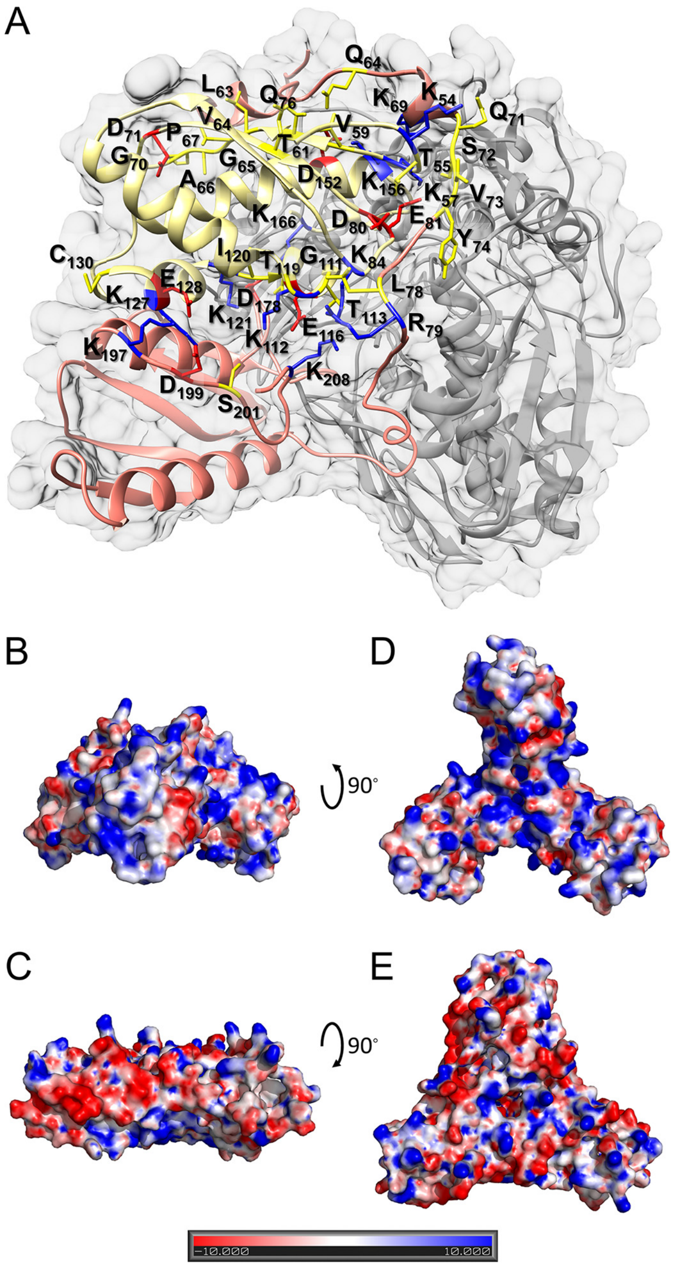

FIGURE 10. **Interface of the $[FXN^{42-210}]_3 \cdot [ISCU]_3$ sub-complex.** *A*, PISA-identified $[FXN^{42-210}] \cdot [ISCU]$ heterodimer interface. Conserved residues within this interface predicted to form hydrogen bonds and salt bridges between the two proteins are shown as *red, blue*, and *yellow sticks* for acidic, basic, and neutral residues, respectively. *B–E*, electrostatic potential of the entire $[FXN^{42-210}]_3 \cdot [ISCU]_3$ sub-complex interface generated using PyMOL. *B* and *C*, ISCU trimer (*B*) and FXN^{42-210} trimer (*C*) in a lock and key arrangement. *D* and *E*, inside view of the interface between ISCU trimer (*D*) and FXN^{42-210} trimer (*E*). Increasing *red* represents increasing negative charge, *white* is neutral charge, and increasing *blue* represents increasing positive charge.

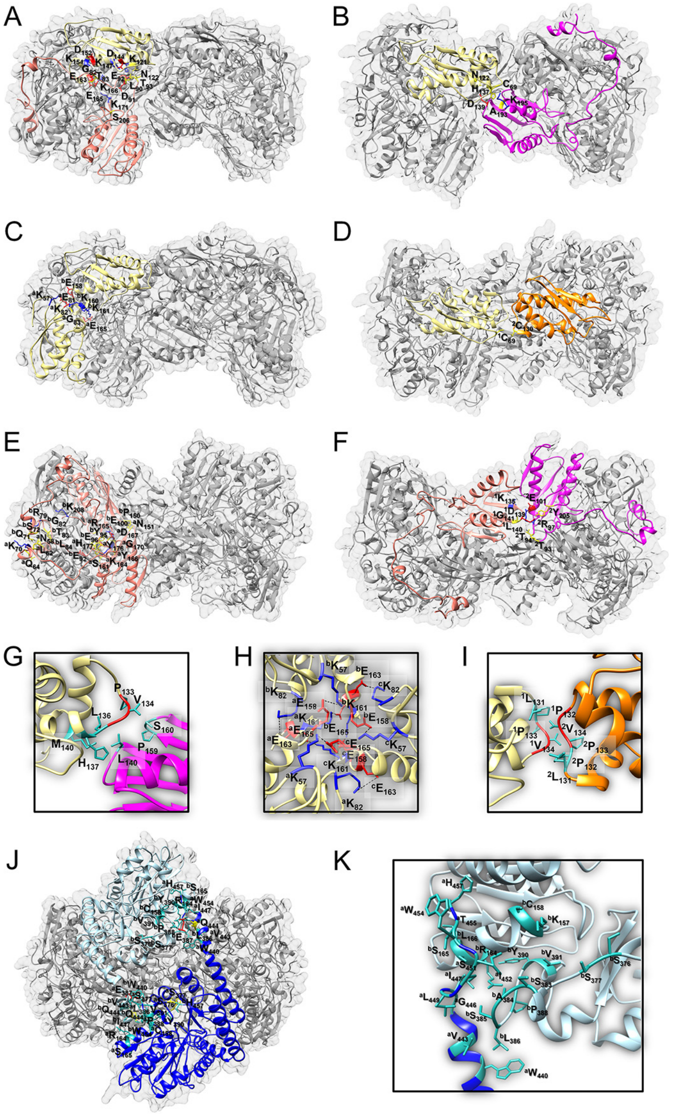

FIGURE 11. **Interfaces within two adjacent $[FXN^{42-210}]_3 \cdot [ISCU]_3$ sub-complexes and within the $[NFS1]_2$ homodimer at the 2-fold axis of the complex.** *A–K*, PISA-identified interfaces with amino acid residues shown as *red, blue, sea blue,* and *yellow sticks* for acidic, basic, hydrophobic, and neutral residues, respectively. *A*, interface between the N terminus of one FXN^{42-210} subunit and one adjacent ISCU subunit within the same $[FXN^{42-210}]_3 \cdot [ISCU]_3$ sub-complex. *B*, interface between one FXN^{42-210} subunit and one ISCU subunit from the adjacent $[FXN^{42-210}]_3 \cdot [ISCU]_3$ sub-complex. *C* and *D*, interface between two ISCU subunits (denoted *a* and *b*) of the same sub-complex (*C*) and two ISCU subunits (denoted *1* and *2*) of adjacent sub-complexes (*D*). *E* and *F*, interface between FXN^{42-210} subunits (denoted *a* and *b*) of the same sub-complex (*E*) and two FXN^{42-210} subunits of adjacent sub-complexes (*F*). *G* and *I*, closer views of *B* and *D*, respectively, show possible hydrophobic interactions involving the PVK motif of ISCU (*red ribbon*) between one ISCU and one FXN^{42-210} subunit (*G*) and between two ISCU subunits of adjacent $[FXN^{42-210}]_3 \cdot [ISCU]_3$ sub-complexes (*I*). *H*, PISA-identified salt bridges at the 3-fold axis of ISCU trimer (*a–c* denote the three subunits). *J*, two symmetrical interface are present between subunits of the NFS1 homodimer; *K* shows hydrophobic residues involved in one of the two NFS1-NFS1 interfaces.

as well as between loops L7 of one subunit and loops L7 and L9 of another subunit (Fig. 11*E*; supplemental Table S3). Interestingly, this interface includes a salt bridge between Glu-100 and Arg-165 (Fig. 11*E*), which is involved in a pathological human mutation, R165C, found in Friedreich ataxia patients (52). The second FXN^{42-210}-FXN^{42-210} interface is formed by two adjacent trimers of FXN^{42-210}, between loop L3 and helix α3 of one FXN^{42-210} subunit in one trimer, and loop L6 of another FXN^{42-210} subunit in the adjacent trimer (Fig. 11*F*; supplemental Table S3). The pair Glu-101–Lys-135, which is invariant in eukaryotes, is predicted to be involved in a salt bridge formation between two adjacent trimers of FXN^{42-210} (Fig. 11*F*).

The NFS1-NFS1 dimer interface with BSA of ~1600 Å^2 (unique interface, sum of the two symmetrical interfaces shown in Fig. 11*J*) is formed by residues conserved among eukaryotes.

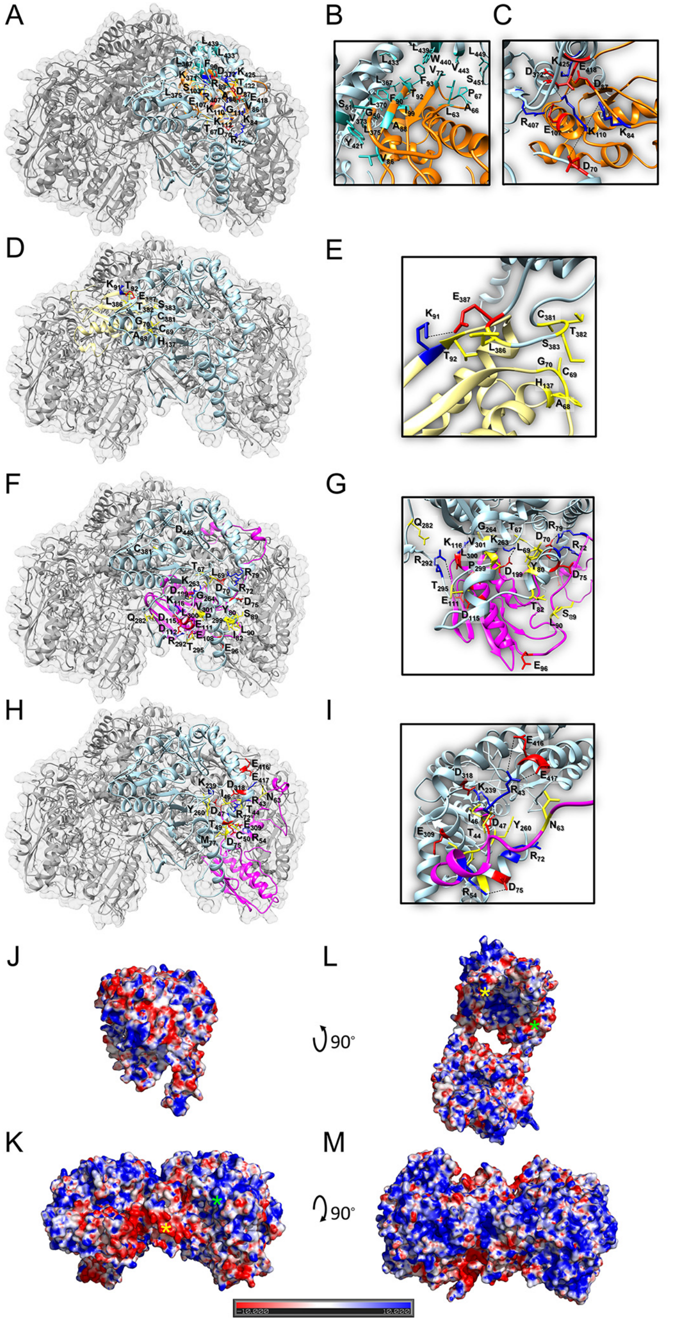

FIGURE 12. **Interfaces between [NFS1]$_2$ homodimer and two adjacent [FXN$^{42-210}$]$_3$·[ISCU]$_3$ sub-complexes at the 2-fold axis of the complex.** *A–I*, PISA-identified interfaces with amino acid residues shown as *red, blue, sea blue,* and *yellow sticks* for acidic, basic, hydrophobic, and neutral residues, respectively. *A* and *D*, interfaces between each subunit of the NFS1 homodimer and ISCU subunits of two adjacent [FXN$^{42-210}$]$_3$·[ISCU]$_3$ sub-complexes. *B* and *C*, hydrophobic interactions (*B*) and salt bridges (*C*) between NFS1 and ISCU subunits at the interface shown in *A*. *E*, salt bridges formed between NFS1 and ISCU subunits at the interface shown in *D*. *F* and *H*, interface between each subunit of the NFS1 homodimer and two FXN$^{42-210}$ subunits of the same [FXN$^{42-210}$]$_3$·[ISCU]$_3$ sub-complex. *G* and *I*, salt bridges between NFS1 and FXN$^{42-210}$ subunits at the interfaces shown in *F* and *H*. *J–M*, electrostatic potential of the entire [FXN$^{42-210}$]$_6$·[ISCU]$_6$·[NFS1]$_2$ sub-complex interface generated using PyMOL. *J* and *K*, [NFS1]$_2$ homodimer (*J*) and two adjacent [FXN$^{42-210}$]$_3$·[ISCU]$_3$ sub-complexes (*K*) are shown in a lock and key arrangement. *L* and *M*, inside view of the interface between the NFS1 heterodimer (*L*) and two adjacent [FXN$^{42-210}$]$_3$·[ISCU]$_3$ sub-complexes (*M*). Increasing *red* represents increasing negative charge; *white* is neutral charge, and increasing *blue* represents increasing positive charge. *K* and *L*, *yellow asterisks* show an acidic patch on FXN$^{42-210}$, including conserved residues Asp-112 and Asp-115 (*K*), and a corresponding basic patch on NFS1, including invariant residues Arg-289 and Arg-R292 (*L*); *green asterisks* show a basic patch formed by FXN$^{42-210}$ residues Arg-43, Arg-53, and Arg-54, together with ISCU conserved residues Lys-84 and Lys-110 (*K*), and a corresponding acidic patch on NFS1, including conserved residues Asp-372, Glu-416, and Glu-417) (*L*).

Four residues in this interface are predicted to form hydrogen bonds between the C-terminal part of one NFS1 subunit, and loops L18 and L19 of the other NFS1 subunit (Fig. 11*J*; supplemental Table S3). Interestingly, other conserved residues involved in this interface are hydrophobic or partially hydrophobic (supplemental Table S3). Hydrophobic interactions between the two NFS1 subunits (Fig. 11, *J* and *K*) create a hydrophobic pocket around the two Fe-S cluster assembly sites of ISCU (Figs. 5, *B* and *D*, and 11*J*).

Each of the two NFS1 subunits in the [FXN$^{42-210}$]$_3$·[ISCU]$_3$·[NFS1]$_2$ sub-complex interacts with two ISCU subunits from the two adjacent ISCU trimers via two distinct interfaces with BSA of ~1285 and 315 Å^2 (average of two recurring interfaces each). The first interface involves one NFS1 subunit and one ISCU subunit in the ISCU trimer immediately underneath (Fig. 12*A*). The flexible N-terminal region as well as helix α9, sheet β10, and helix α13 of NFS1 interact with strand β3, and helix α1 of ISCU (Fig. 12*A*; supplemental Table S3). This interface is predicted to involve salt bridges between NFS1 and ISCU (Fig. 12, *A* and *C*; supplemental Table S3). However, some of the residues involved in this interface are hydrophobic. Residues from strands β1-β3 of ISCU and residues from helices α8 and α13 and loops L15 and L23 of NFS1 may be involved in hydrophobic interactions between the two proteins (Fig. 12*B*; supplemental Table S3). Interestingly, residues Leu-63, Val-72, and Phe-94 of yeast Isu1 (corresponding to the invariant Leu-63, Val-72, and Phe-93 residues of ISCU) were previously shown to be important for Isu1-Nfs1 interactions in yeast (53). The second interface is formed between the active site of one NFS1 subunit, including Cys-381, created by loops L18 and L19, and the active site of one ISCU subunit from the neighboring ISCU trimer, including Cys-69 and His-137, created by loops L2, L4, and L7 (Fig. 12*D*). This interface is predicted to involve mainly hydrogen bonding and one salt bridge between the invariant Glu-387 and Lys-91 of NFS1 and ISCU (Fig. 12*E*).

There are two FXN$^{42-210}$-NFS1 interfaces with BSA of ~1895 and 926 Å^2 (average of two recurring interfaces each), involving the same NFS1 subunit and two different FXN$^{42-210}$ subunits within the same trimer immediately underneath. The first interface involves a flexible N-terminal region as well as loops L13, L14, L18, and L23 of NFS1, and loop L3, helix α3, loop L4, and helix α4 of FXN$^{42-210}$ (Fig. 12*F*; supplemental Table S3). Interestingly, Cys-381 from the active center of NFS1 is located close to negatively charged residues from helix α3 of FXN$^{42-210}$ (Fig. 12*G*), which are predicted to be involved in iron binding (see below). Most of the residues from this interface are invariant in eukaryotes and are predicted to form hydrogen bonds and several salt bridges (Fig. 12*G*; supplemental Table S3). The second FXN$^{42-210}$-NFS1 interface involves invariant residues from NFS1 N-terminal region, loops L12 and L13, and helices α8 and α13, and non-conserved N-terminal residues of FXN$^{42-210}$ (Fig. 12*H*), some of which form hydrogen bonds and salt bridges (Fig. 12*I*; supplemental Table S3).

Surface and charge analysis shows that two adjacent [FXN]$_3$·[ISCU]$_3$ sub-complexes form a groove with one negatively charged patch and one positively charged patch on each side (Fig. 12*K*, *yellow* and *green asterisks*). The corresponding interface formed by the two NFS1 subunits has two patches of opposite charges (Fig. 12*L*, *yellow* and *green asterisks*), suggesting that the electrostatic interactions may contribute to complex formation (Fig. 12, *J–M*).

Proposed [2Fe-2S] Cluster Assembly Site of [FXN$^{42-210}$]$_{24}$·[NFS1]$_{24}$·[ISD11]$_{24}$·[ISCU]$_{24}$ Complex—Two adjacent [FXN$^{42-210}$]$_3$·[ISCU]$_3$ sub-complexes, consisting of two adjacent ISCU trimers bound on top of two adjacent FXN$^{42-210}$ trimers, are present at each of the 2-fold axes of the complex (Figs. 5 and 13). Two ISCU subunits, one from each of the two ISCU trimers (designated trimers *1* and *2*), face each other with their respective [2Fe-2S] coordinating sites formed by the invariant Cys-69, Cys-95, His-137, and Cys-138 residues (Figs. 5*A* and 13, *B* and *C*). These residues are involved in Fe-S cluster coordination in prokaryotic IscU scaffolds (21, 54, 55). In each site, these residues are within ~2–4 Å from each other, suitable to coordinate one [2Fe-2S] cluster (21). The two [2Fe-2S] cluster coordinating sites are above the interface between the two FXN$^{42-210}$ trimers, which is formed by two adjacent subunits from each of the two trimers (designated trimers *1* and *2*). Alignment with two available structures of iron-bound Yfh1^{Y73A} trimer (PDB codes 2FQL and 4EC2) (31, 56) identified potential iron-binding sites that may be implicated in iron transfer to each of the two [2Fe-2S] cluster coordinating sites (Fig. 13, *B* and *C*). The first iron-binding site is in the channel at the 3-fold axis of each FXN$^{42-210}$ trimer, formed by three Asp-167 residues (Asp-143 in Yfh1), one from each subunit of the trimer (*e.g.* trimer *1* in Fig. 13*C*). From this site, iron could move to a second site formed by residues Thr-142 and Ser-157 (Thr-118 and Ala-133 in Yfh1) from one subunit of the opposite FXN$^{42-210}$ trimer (trimer *2* in Fig. 13*C*). In addition, alignment with the [Yfh1]$_{24}$·[Isu1]$_{24}$ complex (32) suggests the presence of a third iron-binding site formed by residues Glu-96, Glu-100, Glu-101, and Asp-104 (His-74, Asp-78, Asp-79, and Asp-82 in Yfh1) of trimer *1*, together with residues Asp-124, Ser-126, and Thr-133 (Asp-101, Glu-103, and Thr-110 in Yfh1) of trimer *2* (Fig. 13*C*). This site is reminiscent of the ferroxidation site of *E. coli* ferritin (Fig. 13*D*) (57); and interestingly, in Yfh1, residues His-74, Asp-78, Asp-79, Asp-82, and His-83 compose the ferroxidation site, and residues Asp-101 and Glu-103 are part of the mineralization site of the protein (28, 58). Alignment of cobalt-bound CyaY monomer (PDB code 2EFF) identified a fourth potential iron-binding site formed by residue Asp-104 (Asp-82 in Yfh1) from trimer *1* and Asp-124 (Asp-101 in Yfh1) from trimer *2*. Four of these sites are present at the 4-fold axis of the complex (Fig. 13*E*) and may constitute the mineralization site of the protein, as described for the Yfh1 24-mer (28, 58).

The PVK motif of Isu1 is important for Yfh1-Isu1 interactions in yeast (50). The PVK motif of ISCU is close to the Fe-S cluster assembly site and may interact with both FXN$^{42-210}$ subunits immediately underneath (*i.e.* in the same [FXN$^{42-210}$]$_3$·[ISCU]$_3$ sub-complex) as well as the adjacent FXN$^{42-210}$ subunit from the opposite [FXN$^{42-210}$]$_3$·[ISCU]$_3$ sub-complex (Figs. 11, *G* and *I*, and 13*B*). Moreover, PISA analysis predicts hydrogen bonding between the two opposite ISCU subunits involving Cys-69–Cys-130 (Fig. 11*D*), which may contribute to the stability of the cluster assembly site.

Docking of 24 NFS1 monomers into the EM density map of the refined 3D model results in the presence of one symmetric NFS1 dimer resting on top of two [FXN$^{42-210}$]$_3$·[ISCU]$_3$ sub-complexes at each of the 2-fold axes of the complex (Fig. 5, *B* and *D*). The invariant catalytic Cys-381 of NFS1 is on a flexible loop at 6.4 ± 1.8 Å from Cys-69 and 10.3 ± 1.4 Å from Cys-138 of ISCU (average of eight distances measured between the backbone α-carbons of Cys-381 and Cys-69 or C-381 and Cys-138 in the simulated half-structure of the complex) (Figs. 5*D* and 13, *A–C*). Cys-69 and Cys-138 are proposed acceptors of the persulfide formed on Cys-381 of NFS1 (21, 23, 25). The fold of the NFS1 and ISCU monomers is very similar to the fold of *Archaeoglobus fulgidus* and *E. coli* IscS and IscU monomers (Fig. 14, *A–C*). However, when the *A. fulgidus* [IscS]·[IscU] heterodimer is aligned with the [NFS1]·[ISCU] heterodimer, NFS1 and IscS overlap each other, whereas ISCU is rotated ~90° relative to IscU on the same plane, which brings the Fe-S cluster coordination site of ISCU closer to the NFS1 flexible loop (Fig. 14, *D* and *E*). This configuration is supported by cross-links between NFS1 and ISCU as well as NFS1 and FXN$^{42-210}$ (Fig. 14*F*).

Discussion

Although FXN$^{81-210}$ and [NFS1]·[ISD11] have been shown to work together to promote the assembly of new Fe-S clusters on the scaffold ISCU (12, 13), the architecture of the complex formed by these proteins is not yet defined, and an integrated mechanism for the concerted delivery of iron and sulfur to ISCU is not yet known. To gain new information, we focused on FXN$^{42-210}$, the longest known isoform of human frataxin, which forms oligomers that can participate in Fe-S cluster assembly using a more stable mode of interaction with [NFS1]·[ISD11] and ISCU as well as a higher iron binding capacity as compared with monomeric FXN$^{81-210}$ (14). We reconstituted in *E. coli* and purified a stable and functional macromolecular complex consisting of stoichiometric amounts of FXN$^{42-210}$, NFS1, ISD11, and ISCU. Then, via negative staining EM single-particle analysis, we obtained a 3D model of the complex at a resolution of ~14 Å. Segmentation of the EM density map of the 3D model, followed by sequential docking of [FXN$^{42-210}$]$_3$·[ISCU]$_3$ sub-complexes and NFS1 monomers into the available volumes, and by modeling of ISD11 monomers at the surface of the complex, led to the proposed structure of the [FXN$^{42-210}$]$_{24}$·[NFS1]$_{24}$·[ISD11]$_{24}$·[ISCU]$_{24}$ complex. This structure fits into the EM density map of the 3D model without steric clashes and in a manner consistent with the measured 1:1:1:1 stoichiometry of the four protein components of the complex. The structure also fulfills distance constraints obtained from chemical cross-linking analysis at all main protein-protein interfaces present at the 2-, 3-, and 4-fold axes of the complex. These interfaces are compatible with the formation of hydrogen bonds, salt bridges, and hydrophobic interactions, often involving conserved residues. Finally, the structure of the complex is supported by the presence of 24 Fe-S cluster assembly centers, where the arrangement of cluster

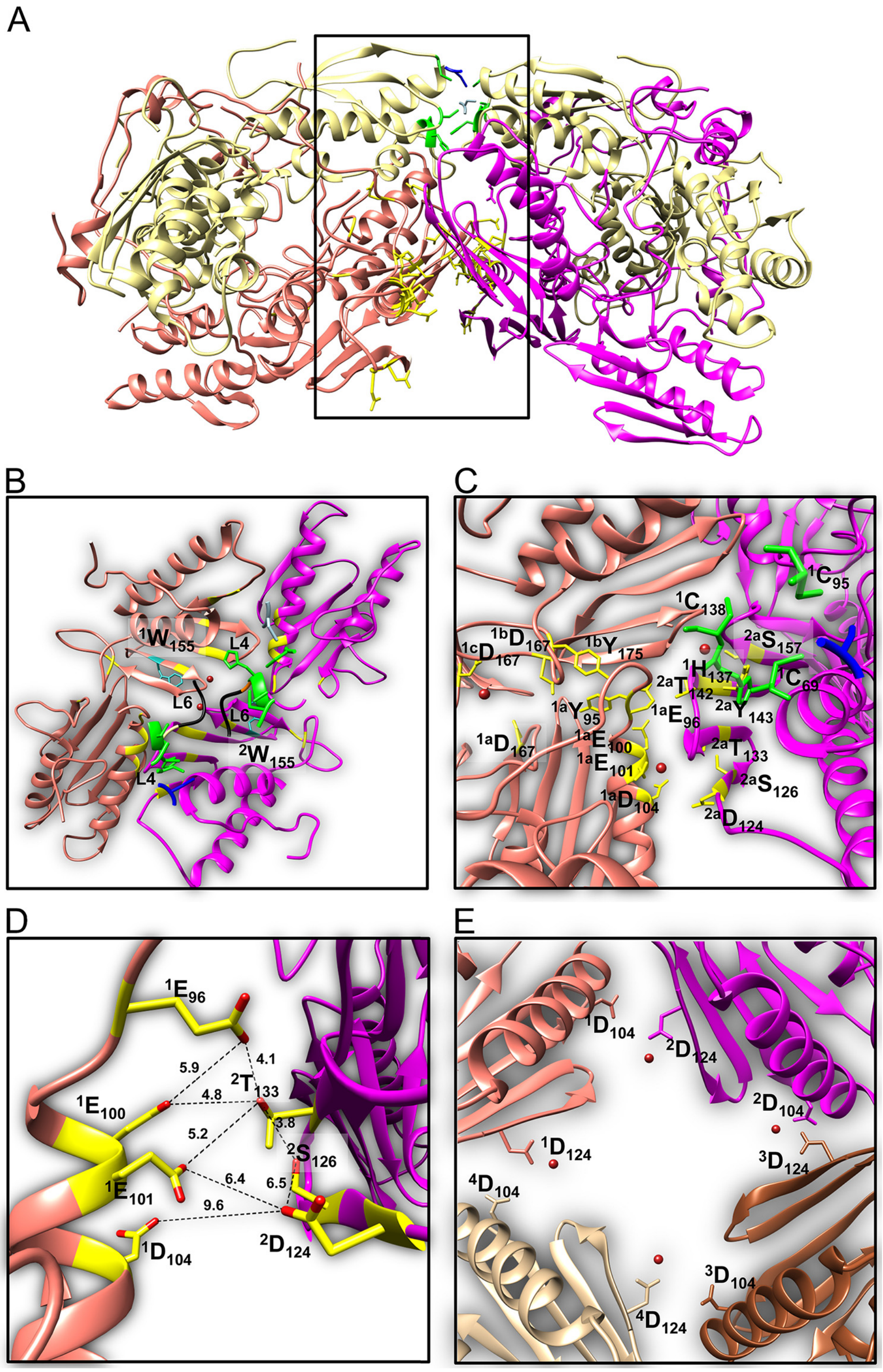

FIGURE 13. **Fe-S cluster assembly center of the human four-protein complex.** *A*, *ribbon* representation of the Fe-S cluster assembly center formed by two adjacent $[\text{FXN}^{42-210}]_3\cdot[\text{ISCU}]_3$ sub-complexes and one $[\text{NFS1}]_2\cdot[\text{ISD11}]_2$ sub-complex at the 2-fold axis of the complex; for the two NFS1 subunits, only the Cys-381 residues are shown as a *light blue* and a *blue stick*; ISD11 subunits are not shown (see also Fig. 5*B*). *B*, position of the PVK motifs (shown as *black ribbons*) of ISCU subunits relative to each of the two Fe-S cluster assembly centers; Trp-155 of FXN^{42-210} is shown as a *light blue stick*; FXN^{42-210} residues involved in iron binding are highlighted in *yellow*. *C*, proposed FXN^{42-210} iron-binding sites modeled as described under "Results." The *numbers 1* and *2* denote two adjacent FXN^{42-210} or ISCU trimers; the *letters a–c* denote different subunits of FXN^{42-210} or ISCU trimer *1* or *2*. For ISCU, only the Fe-S cluster coordinating residues are shown as *green sticks*. For NFS1, only the catalytic Cys-381 is shown as a *blue stick*. FXN^{42-210} residues involved in iron binding are shown as *yellow sticks*. *D*, putative ferroxidation site formed by two FXN^{42-210} subunits from the two adjacent $[\text{FXN}^{42-210}]_3\cdot[\text{ISCU}]_3$ sub-complexes at the 2-fold axis of the complex. *E*, putative iron mineralization sites formed by four FXN^{42-210} subunits from four adjacent $[\text{FXN}^{42-210}]_3\cdot[\text{ISCU}]_3$ sub-complexes at the 4-fold axis of the complex. Iron atoms were modeled as described under "Results." The *numbers 1–4* denote four adjacent FXN^{42-210} trimers.

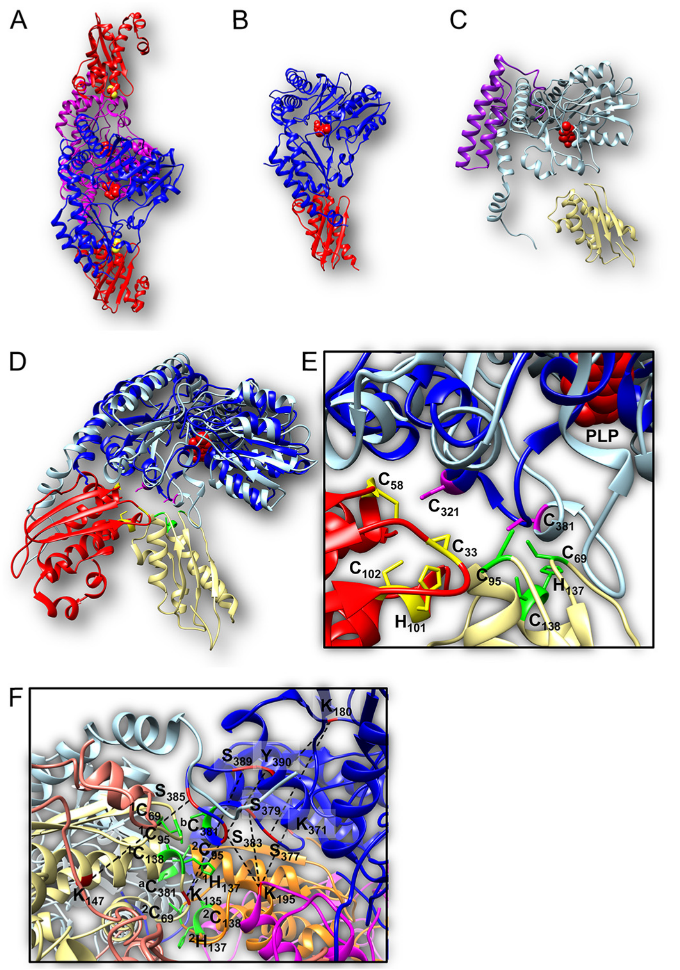

FIGURE 14. **Comparison of bacterial and human Fe-S cluster assembly complexes.** *A–C, ribbon* representation of the *A. fulgidus* $[IscS]_2$·$[IscU]_2$ complex (PDB code 4EB5) (*A*), the *E. coli* [IscS]·[IscU] complex (PDB code 3LVL) (*B*), and the [NFS1]·[ISD11]·[ISCU] heterotrimer from the human complex (*C*). *D*, alignment of the [IscS]·[IscU] heterodimer with the [NFS1]·[ISCU] heterodimer shows the different positions of IscU (*red ribbon*) and ISCU (*yellow ribbon*) relative to the flexible loop and catalytic Cys of IscS (*blue ribbon*) and NFS1 (*light blue ribbon*). The pyridoxal 5′-phosphate cofactor is shown in *red*. *E*, close view of the flexible loops of IscS (*blue ribbon*) and NFS1 (*light blue ribbon*), with Cys-321 of IscS and Cys-381 of NFS1 shown as *magenta sticks*, relative to the positions of the Fe-S cluster coordinating residues of IscU (*red ribbon*) and ISCU (*yellow ribbon*), shown as *yellow* (IscU) and *green* (ISCU) *sticks*. *F, ribbon* representation of the Fe-S cluster assembly center formed by one NFS1 dimer resting on top of two adjacent $[FXN^{42-210}]_3$·$[ISCU]_3$ sub-complexes at the 2-fold axis of the complex with Fe-S cluster coordinating residues of the two ISCU subunits shown as *green sticks* (*1* and *2* denote the two ISCU subunits), and the flexible loops of the two NFS1 subunits with the catalytic Cys-381 residues shown as a *green sticks* (*a* and *b* denote the two NFS1 subunits). The arrangement fulfills the distance constraints set by FXN^{42-210}-NFS1 cross-links *K195–K171, K195–S379,* and *K195–S383* (supplemental Table S2*f*, p. 1), ISCU-NFS1 cross-links *K147–S385, K135–S389,* and *K135–Y390* (supplemental Table S2*g*, pp. 1 and 3), and NFS1-NFS1 cross-links *K180–S377* and *K180–S379* (supplemental Table S2*c*, p. 1). Cross-links are shown as *dotted lines*; cross-linked residues are highlighted in *red*.

coordinating residues of ISCU relative to the catalytic flexible loop of NFS1 and the iron-binding residues of FXN^{42-210} not only recapitulate the known mechanism for sulfur donation from NFS1 to ISCU but also provide a path for iron donation from FXN^{42-210} to ISCU.

At the center of the structure, eight symmetric FXN^{42-210} trimers form a cubic 24-mer (Fig. 4*D*). The frataxin structure can be adapted to oligomerize as evidenced by the ability of bacterial CyaY to form tetramers and of yeast Yfh1 to form trimers at low iron to protein ratios (≤2:1) (28, 59), and by the ability of both CyaY and Yfh1 to form higher order oligomers at increasing iron to protein ratios (5, 27, 56). Unlike CyaY or Yfh1, FXN^{42-210} oligomerizes in an iron-independent manner in human, yeast, and bacterial cells (7), which is also an intrinsic property of the frataxin structure because certain point mutations result in iron-independent oligomerization of Yfh1 both in yeast and bacterial cells (29).

One symmetric ISCU trimer binds on top of each of the eight trimers that form the FXN^{42-210} 24-mer. IscU-type scaffolds have been shown to exist in monomeric or oligomeric states in the absence of protein partners (6, 54, 55, 60, 61). However, binding of a distribution of Isu1 monomer, dimer, and trimer to $Yfh1^{Y73A}$ 24-mer resulted in the assembly of a complex in which one symmetric Isu1 trimer was bound on top of each of the eight trimers present in the $Yfh1^{Y73A}$ 24-mer, in a manner that created 24 [2Fe-2S] cluster assembly sites (32). Similarly, conformational changes leading to stabilization of bacterial IscU were observed upon binding of IscU to the co-chaperone HscB (62). These previous data and our present results together indicate that binding of ISCU to its protein partners may result in new conformations required for ISCU activity in Fe-S cluster assembly.

Two adjacent $[FXN^{42-210}]_3$·$[ISCU]_3$ sub-complexes are present at each of the 2-fold axes of the complex, such that two ISCU subunits, one from each sub-complex, face each other with their respective [2Fe-2S] coordinating sites (Figs. 5, *A* and *D*, and 13*A*). Each of these sites is close to iron-binding sites formed by the two adjacent FXN^{42-210} trimers (trimer *1* and trimer *2*) underneath the two ISCU trimers (Fig. 13, *B* and *C*). Furthermore, one symmetric NFS1 dimer binds on top of the two adjacent $[FXN^{42-210}]_3$·$[ISCU]_3$ sub-complexes, which positions the flexible loop and catalytic Cys-381 of each NFS1 subunit close to each of the two [2Fe-2S] cluster assembly sites of ISCU (Figs. 5, *B* and *D*, and 13*C*). In this way, amino acids involved in iron and sulfur donation and coordination are arranged in close proximity as would be required for the safe handling of potentially toxic iron and sulfur atoms.

Biochemical and structural studies of bacterial, yeast, and mammalian Fe-S cluster assembly complexes have led to a conserved mechanism for sulfur donation from the cysteine desulfurase to the scaffold (3, 13, 22, 23, 26). This mechanism predicts that the flexible loop of NFS1 must first move close to the L-cysteine substrate-binding site to enable formation of persulfurated Cys-381 (10, 20, 21, 23), and then move close to the Fe-S cluster assembly site to enable sulfur transfer from persulfurated Cys-381 to ISCU (10, 26). It was also shown that binding of the shorter frataxin isoform, FXN^{81-210}, to the $[NFS1]_2$·$[ISD11]_4$·$[ISCU]_2$ complex accelerates persulfide formation on NFS1 (23–25). This led to a proposed model of FXN^{81-210}-dependent activation of the complex whereby FXN^{81-210} binding would stabilize a coil conformation in ISCU, resulting from unwinding of its C-terminal helix, which would bring Cys-138 of ISCU closer to Cys-381 of NFS1 and facilitate sulfur transfer. Addition of iron and reducing equivalents would then somehow result in [2Fe-2S] cluster formation on ISCU (23). The structure of each $[[FXN^{42-210}]_3$·$[ISCU]_3]_2$·

$[NFS1]_2$ sub-complex in our model is consistent with a similar although simpler mechanism. Cys-381 of NFS1 is at ~11 Å from the NFS1 substrate-binding site and at ~9 Å from Cys-138 of ISCU. This suggests that the flexible loop of NFS1 would have to move toward the substrate-binding site to allow formation of the persulfurated Cys-381; however, only small conformational changes in ISCU would be required to enable sulfur transfer from Cys-381 to Cys-138 (Figs. 5*D* and 14, *D* and *E*).

Our structure may also help to explain how human frataxin may serve as both the activator of NFS1 and the iron donor, which remains unclear (13, 23). In the context of the yeast $[Nfs1]_2 \cdot [Isd11]_2 \cdot [Isu1]_2 \cdot [Yfh1]_2$ and human $[FXN^{81-210}]_2 \cdot [NFS1]_2 \cdot [ISD11]_4 \cdot [ISCU]_2$ complexes, one monomer of Yfh1/FXN^{81-210} is thought to bind in a pocket between Nfs1/NFS1 and Isu1/ISCU through the conserved frataxin iron-binding surface (8, 13). However, it has been suggested that this mode of frataxin binding could interfere with sulfur transfer (26) as well as iron entry (13). In contrast, the positioning of ISCU relative to FXN^{42-210} and NFS1 in our structure allows for FXN^{42-210} and NFS1 to simultaneously bind to ISCU and to stimulate Fe-S cluster synthesis (Fig. 1, *A–H*), consistent with our previous observation that ISCU and [NFS1]·[ISD11] can independently or simultaneously bind to oligomeric FXN^{42-210} in solution (7). Because oligomeric FXN^{42-210} is normally present in human mitochondria (7), it may normally serve as a platform to reconstitute active [2Fe-2S] assembly sites through recruitment of [NFS1]·[ISD11]·[ISCU] sub-complexes. A comparison between the arrangement of one [NFS1]·[ISD11]·[ISCU] sub-complex from our structure with the *A. fulgidus* $[IscS]_2 \cdot [IscU]_2$ and *E. coli* [IscS]·[IscU] complexes (Fig. 14, *A–C*) suggests that binding of [NFS1]·[ISD11]·[ISCU] to oligomeric FXN^{42-210} changes the orientation of ISCU and thus the position of the cluster coordinating site relative to the catalytic loop of NFS1 (Fig. 14, *D* and *E*). Binding of [NFS1]·[ISD11]·[ISCU] to oligomeric FXN^{42-210} may also induce conformational changes that make the substrate-binding site of NFS1 more accessible to L-cysteine, thereby activating the cysteine desulfurase activity (10). Modeling of previously identified iron- or cobalt-binding sites of Yfh1 or CyaY into our structure further suggests a mechanism for iron transfer from FXN^{42-210} to ISCU, which is fully contained within one $[[FXN^{42-210}]_3 \cdot [ISCU]_3]_2 \cdot [NFS1]_2$ sub-complex at each of the 2-fold axes of the complex (Figs. 5, *B–D*, and 13, *B–E*). A path for iron delivery to one of the two Fe-S cluster assembly sites in the sub-complex could go from the three Asp-167 residues at the 3-fold axis of FXN^{42-210} trimer *1* to the site formed by Thr-142 and Ser-157 of FXN^{42-210} trimer *2* and to His-137 in the [2Fe-2S] coordinating site of ISCU trimer *1* (Fig. 13*C*). FXN^{42-210} trimer *1* residues, Tyr-175 and Glu-96, may be involved in the transfer of iron from the 3-fold axis of trimer *1* to the second site on trimer *2*, and Tyr-143 of trimer *2* may help the transfer of iron from this site to His-137 of ISCU trimer *1*. The structure also suggests that in the absence of ISCU, FXN^{42-210}-bound iron could take a different path, from the 3-fold axis of trimer *1* to the putative ferroxidation site formed by trimer *1* together with trimer *2* (via Tyr-95 and Glu-96 of trimer *1*), followed by transfer to the mineralization site at the 4-fold axis of the complex (Fig. 13, *C–E*). This alternate path may serve to detoxify FXN^{42-210}-bound iron that is not utilized (Fig. 13, *B–E*), as proposed previously (63).

The model described above is consistent with several previous observations. The PVK motif of Isu1 was shown to be important for Isu1-Yfh1 interactions in yeast (50). In our structure, the PVK motif of ISCU is close to the Fe-S cluster assembly site and, based on both cross-linking data and PISA interface analysis, it may interact with both the flexible loop of NFS1 at a distance of ~7–8 Å, which contains the catalytic Cys-381, as well as with loops L4 and L6 of FXN^{42-210} at a distance of ~5 Å, which contain the iron-binding site formed by Thr-142 (loop L4) and Ser-157 (loop L6) (Fig. 13*B*). These interactions may contribute to the stability of the cluster assembly site and facilitate sulfur and iron delivery to ISCU. In addition, it was previously shown that replacement of Leu-63, Val-72, or Phe-94 of yeast Isu1 (corresponding to Leu-63, Val-72, and Phe-93 of human ISCU) with alanine residues affects Isu1 interactions with [Nfs1]·[Isd11] (50, 53). It was suggested that residues Leu-63, Val-72, and Phe-94 of Isu1 are critical for interaction with hydrophobic residues of Nfs1, Met-482, Pro-478, and Leu-479 (Met-442, Pro-438, and Leu-439 in NFS1) (53). Indeed, Leu-63, Val-72, and Phe-93 of ISCU in our structure are close to hydrophobic residues of NFS1, including Met-436, Pro-438, and Leu-439 but also Trp-440, Met-442, and Val-443, which are located on the C-terminal portion of NFS1 (Fig. 12*B*). In addition, a G50E mutation in ISCU was shown to affect ISCU interactions with NFS1 (64). In our structure, Gly-50 is located on the flexible portion of the ISCU N terminus, close to helix $\alpha13$ of NFS1 (Fig. 12*B*). A Gly to Glu substitution may reduce the flexibility of the N-terminal portion of ISCU and may affect formation of hydrophobic interactions with NFS1. Finally, certain frataxin mutations identified in Friedreich ataxia patients are located in the β-sheet region of the protein and affect interactions of frataxin with other protein partners (52, 65). In particular, a W155R mutation disrupted interactions of FXN^{81-210} with the $[NFS1]_2 \cdot [ISD11]_4 \cdot [ISCU]_2$ complex (52, 65) but did not affect the ability of FXN^{42-210} to interact with NFS1 *in vivo* (19). *In vitro*, however, the W155R mutation affected the ability of both FXN^{42-210} and FXN^{81-210} to stimulate the cysteine desulfurase activity of NFS1 and to promote Fe-S cluster synthesis (19). We proposed that in the context of oligomeric FXN^{42-210}, Trp-155 might play a role independent of (or not limited to) providing a binding site for the [NFS1]·[ISD11] and/or ISCU. Based on the structure presented here, we further propose that the W155R and other pathogenic mutations in the β-sheet of FXN^{42-210} (N146K, I154F, and R165C) may interfere with sulfur transfer from NFS1 to ISCU. In our model, residues in the β-sheet of FXN^{42-210} are within 5 Å from the PVK motif of ISCU (Fig. 13*B*). Any disturbance to the PVK motif may affect both Cys-381 in the NFS1 flexible loop, at ~7–8 Å from the PVK motif, as well as His-137 and Cys-138 of ISCU, which are in the same flexible loop as Pro-133, Val-134, and Lys-135.

Thus, the structural model of the complex presented in this paper provides a path for concerted iron and sulfur donation from FXN^{42-210} and NFS1 to ISCU, and it also helps to explain the effects of mutations in conserved amino acids of the three proteins (50, 53, 64), including pathogenic mutations in frataxin involved in Friedreich ataxia (52, 65).

Experimental Procedures

DNA Constructs Used for Four-protein Co-expression in E. coli—Two DNA fragments encoding residues 35–168 of ISCU, which comprise the predicted mature form of this protein (66), and residues 42–210 of FXN, which comprise the longest native isoform of FXN (7), were PCR-amplified and cloned into the pET-52b(+) 3C/LIC vector using the LIC Duet Adaptor and LIC Cloning kit (Novagen) according to the manufacturer's protocol. This cloning enables the simultaneous expression of ISCU and of FXN^{42-210} with an N-terminal Strep·Tag® II. Two DNA fragments corresponding to residues 56–458 of NFS1 and 6–92 of ISD11, comprising the predicted mature forms of these proteins (6, 38), were respectively cloned into the BglII and HindIII sites and the NcoI and EcoRI sites of the pCDFDuet-1 vector (Novagen). This cloning enables the simultaneous expression of ISD11 and of NFS1 with an N-terminal His_6 tag. The two plasmids encoding FXN^{42-210} and ISCU and also NFS1 and ISD11 were co-transformed in the *E. coli* strain BL21 (DE3) (Novagen) for four-protein co-expression.

Purification of Four-protein Complex—*E. coli* cells were grown at 25 °C in 2 liters of Luria broth containing 100 μg/ml ampicillin and 25 μg/ml streptomycin. Protein expression was induced at $A_{600} = 0.6$ with 0.5 mM isopropyl β-D-1-thiogalactopyranoside (Thermo Fisher Scientific) and growth continued at 15 °C for ~18 h. Cells were harvested and disrupted by sonication in 50 mM NaH_2PO_4, pH 8.0, 300 mM NaCl, 10 mM imidazole, containing 1 tablet/50 ml of complete protease inhibitor mixture EDTA-free (Roche Diagnostics). The four-protein complex was isolated from total bacterial cell extract using four consecutive chromatography steps, which included nickel affinity chromatography (5 ml-HiTrap nickel column), preparative size-exclusion chromatography (16-mm × 60-cm column packed with Sephacryl S-300 support), streptavidin-Sepharose™ affinity chromatography (1 ml of StrepTrap™ HP column), and preparative size-exclusion chromatography as above (GE Healthcare). The complex was eluted from the HiTrap nickel column using a 50–150 mM imidazole gradient in buffer containing 50 mM NaH_2PO_4, pH 8.0, 300 mM NaCl. Fractions containing all four proteins were analyzed by Sephacryl S-300 size-exclusion chromatography in buffer containing 50 mM Tris-HCl, pH 8.0, 150 mM NaCl (TN150). Fractions containing all four proteins were loaded on a StrepTrap™ HP column, and the complex was eluted with buffer containing 20 mM NaH_2PO_4, pH 7.4, 150 mM NaCl, 6 mM KCl, 2.5 mM *d*-desthiobiotin. Fractions containing the complex were finally analyzed by Sephacryl S-300 size-exclusion chromatography in TN150 buffer. The four-protein complex was stable and soluble in this buffer. The yield of purified complex was ~2 mg/liter bacterial culture, which could be increased to ~6 mg/liter bacterial culture when we used two StrepTrap™ HP columns in tandem for the third purification step. Protein concentrations were routinely determined using a BCA kit (Thermo Fisher Scientific) and are expressed as total protein.

SDS-PAGE and Mass Spectrometry—For reducing or non-reducing SDS-PAGE, protein samples were mixed v/v with 2× Laemmli buffer in the absence or presence of β-mercaptoethanol (350 mM final concentration), which was added freshly to the buffer from a 14.3 M stock solution. Samples were heated at 90 °C for 10 min and analyzed on 18% Criterion™ precast gels (Bio-Rad). For mass spectrometric analysis of protein bands, samples were analyzed under non-reducing conditions as described above, and the gel was stained with Bio-Safe Coomassie G-250 stain (Bio-Rad). Bands of interest were excised and proteins digested *in situ* with trypsin, and the extracted peptides were identified by nano-flow liquid chromatography electrospray tandem mass spectrometry as described previously (32).

Amino Acid Analysis—This analysis was performed at the AAA Service Laboratory Inc., Damascus, OR. Aliquots of fractions containing complex eluted from the Sephacryl S-300 size-exclusion chromatography were hydrolyzed in 6 N HCl, 2% (v/v) phenol for 22 h at 110 °C. After hydrolysis, samples were dried, resuspended in 100 μl of sampling buffer (sodium citrate, pH 2.20), and injected onto a Hitachi L8900 amino acid analyzer, using post-column ninhydrin derivatization.

Dynamic Light Scattering—Measurements were performed on the *Saccharomyces cerevisiae* $Yfh1^{Y73A}$ 24-mer and $[Yfh1]_{24}\cdot[Isu1]_{24}$ complex, the horse spleen ferritin 24-mer (Sigma), and the human four-protein complex. Each protein sample (~0.2 mg/ml) was analyzed using a DynaPro Molecular Sizing Instrument and Dynamics Version 6 software (Protein Solutions, Inc. NJ) as described previously (32).

Fe-S Cluster Assembly Assays—These assays were performed anaerobically as described previously (7).

Iron Measurements—Iron was measured at the Metals Laboratory, Mayo Clinic, using an inductively coupled plasma mass spectrometer in collision cell mode as described previously (32).

Transmission Electron Microscopy and Single Particle Analysis—Fractions freshly eluted from the Sephacryl S-300 column were diluted to 0.1–0.2 mg of protein/ml in TN150 buffer. Carbon-coated copper grids (400 mesh, EMS) were glow-discharged for 30 s using a DV-502A vacuum evaporator (Denton Vacuum Inc.). After optimization, protein concentrations between 0.2 and 0.3 mg/ml were found to give the best distribution of particles on the grids. Each grid was first preincubated for 1 min on a 20-μl TN150 buffer drop on Parafilm M® (Bemis Co., Inc.). Excess buffer was blotted, and a 10-μl drop of protein sample was placed on the grid for ~2 min. Excess protein sample was blotted, and the grid was then washed two times by placing a 7-μl drop of sterile water on the grid for 1 min. Excess water was blotted, and the grid was stained with 5 μl of 1% (w/v) uranyl acetate for 5 and 30 s by successively placing two separate drops of uranyl acetate on the grid, with excess stain drawn off after each application. The grid was then left to dry on forceps for at least 30 min and stored at room temperature. Electron micrographs were collected at the University of Minnesota Characterization Facility using an FEI Tecnai G^2 F30 field emission gun cryo-transmission electron microscope with acceleration voltage at 300 kV equipped with a 4k × 4k ultrascan CCD camera (4096 × 4096 pixels) with an

Electron Energy-Loss Gatan imaging filter. Images were collected at a defocus range from −0.2 to −3.0 μm and at a magnification of 115,000-fold (1.034 Å/pixel). The EMAN2 software package (42) was used to perform contrast transfer function correction and to further process the images to generate initial and refined 3D models of the complex. To assess the presence of symmetry, structure factors were calculated from the EM density map of a refined 3D model without symmetry applied, and a self-rotation function was calculated by POLARRFN of the CCP4 package (43). Similar calculations were completed using the EM density map of a refined 3D model with 432 symmetry applied. We used the PDBe FSC server to calculate and plot the FSC curve for the refined 3D models described above. For each model, the program calculated the FSC curve from two reconstructions generated in EMAN2 using the even or odd half of the particle data set (42). The program also provided the resolution of the reconstruction measured where the FSC curve crosses correlation values of 0.5, 0.333, or 0.143, as well as the resolution based on the 3-σ criterion and the 1/2 bit criterion (45).

Docking of Structures into the EM Density Maps of the 3D Models—A homology model of the FXN$^{42-210}$ monomer was generated based on the x-ray crystal structure of one subunit of the Yfh1^{Y73A} trimer (PDB code 3OEQ) (56) using the I-TASSER web resource (67). A model of the FXN$^{42-210}$ trimer was then generated by aligning three FXN$^{42-210}$ monomers with the N-terminal region (residues 42–93) removed, with the x-ray crystal structure of the Yfh1^{Y73A} trimer. Homology models of ISCU and NFS1 monomers were generated based on available crystal and NMR structures of bacterial orthologues using the I-TASSER web resource. Then, a model of ISCU trimer was generated by aligning three ISCU monomers with the N-terminal region (residues 35–50) removed with the Isu1 trimer structure from the 3D model of the yeast $[\text{Yfh1}]_{24}\cdot[\text{Isu1}]_{24}$ complex (32). As no structures were available for ISD11, a model of the ISD11 monomer was generated based solely on the ISD11 primary amino acid sequence using the I-TASSER web resource. The pyridoxal 5′-phosphate co-factor was modeled into NFS1 based on the *A. fulgidus* $[\text{IscS}]_2\cdot[\text{IscU}]_2$ complex structure (PDB code 4EB5). The quality of each model was assessed from the model's Ramachandran plot and ProQ-Protein Quality Predictor measures. Quality parameters for each of the models are summarized in supplemental Table S4. The program Chimera (46) was used to segment the EM density map of the refined 3D model obtained by negative staining transmission EM and single particle analysis and to visualize and dock structures into the segmented map. FXN$^{42-210}$ and ISCU trimers were docked both separately or together as a $[\text{FXN}^{42-210}]_3\cdot[\text{ISCU}]_3$ sub-complex, which yielded similar cross-correlation functions, and the latter mode of docking was selected. NFS1 was docked as individual monomeric units. Volumes of the EM map predicted to be occupied by ISD11 were at the surface of the refined 3D model and were not sufficiently delineated from the background to enable docking of ISD11 structures into the segmented map. Therefore, based on the ISD11/NFS1 stoichiometry of ~1:1 measured in the complex, 24 ISD11 monomers were modeled on the surface of the complex structure guided by the cross-linking data; however, ISD11 monomers were not included in the simulations described below.

Molecular Dynamics Flexible Fitting for Docked Structures—Aided by cross-linking data, the FXN$^{42-210}$ and ISCU N termini (residues 42–93 and 36–50) were manually added to the docked structures and modeled into nearby unoccupied volumes of the EM map of the refined 3D model with 432 symmetry applied. The EM map was then converted to Situs format to enable rigid-body docking of the entire complex structure into the EM map prior to performing molecular dynamics simulations and energy minimizations. We were unable to simulate the entire structure containing >100,000 atoms due to the computational limitations of our setup. To overcome this problem, only one-half of the structure, consisting of six NFS1 dimers docked on top of four $[\text{FXN}^{42-210}]_3\cdot[\text{ISCU}]_3$ sub-complexes, was subjected to molecular dynamic simulations and energy minimizations using NAnoscale Molecular Dynamics, NAMD 2.10 (68), followed by structure improvement iterations with the program Coot (69), as described previously (32). This process yielded a structure that closely matched the $[\text{FXN}^{42-210}]_3\cdot[\text{ISCU}]_3$ and NFS1 homology models used for the initial docking, with a Ramachandran plot showing 91% of the residues in the favorable region, a MolProbity score of 2.81 with only 1.2% β-carbon deviations >0.25 Å (70), and a Z score of ≤11, which together indicated that the simulated structure had reasonable geometry (69). For the purpose of visualizing the entire complex structure, the simulated half was aligned with itself into the EM density map, followed by structure improvement iterations with the program Coot to resolve small steric clashes between NFS1 subunits at the interface between the two halves of the structure.

Chemical Cross-linking, Limited Proteolysis, and Tandem Mass Spectrometry—For the initial characterization of the complex, we used the water-soluble cross-linker, DTSSP (Thermo Fisher Scientific), which consists of an eight-atom spacer arm with an amine-reactive NHS ester at each end and a central disulfide bond that can be cleaved with reducing agents. Four-protein complex freshly eluted from the Sephacryl S-300 column (1–2 mg of total protein in 1 ml of TN150 buffer) was incubated with DTSSP at a protein/DTSSP molar ratio of 1:60 for 30 min at room temperature, and the reaction was quenched by the addition of 1 M Tris-HCl buffer, pH 7.5, to a final concentration of 20 mM. This sample was fractionated again on the Sephacryl S-300 column, and fractions were analyzed by SDS-PAGE on an 18% Criterion Tris-HCl precast gel (Bio-Rad), in the presence or absence of the reducing agent β-mercaptoethanol. To perform EM studies and to identify protein-protein interfaces in the complex, we used the water-soluble unbreakable cross-linker, BS^3 (Thermo Fisher Scientific), a monobifunctional N-hydroxysuccinimide ester that reacts primarily with the ϵ-amino group of the side chain of Lys residues and the α-amino group of the N terminus of polypeptides and more weakly with the OH group of the side chains of Tyr, Thr, or Ser residues (71, 72). Complex freshly eluted from the StrepTrap™ HP affinity column (1 ml containing 1–2 mg of total protein) was incubated with BS^3 at a protein/BS^3 molar ratio of 1:100 for 30 min at room temperature, and the reaction was quenched with 20 mM Tris-HCl buffer, pH 7.5. The cross-linked complex was re-isolated via Sephacryl S-300 size-exclusion chromatography and used for dynamic light scattering and EM studies or limited proteolysis coupled with mass spectrometry studies. For the latter set of studies, 20 μg of cross-linked or uncross-linked complex freshly eluted from the Sephacryl S-300 column was incubated with 1 μg of the endoproteinase GluC (New England Biolabs) in a total volume of 40 μl at 37 °C. GluC selectively cleaves peptides C-terminal to glutamic residues and, at a slower rate, aspartate residues. As analyzed by SDS-PAGE, a time course of digestion showed that uncross-linked complex was completely digested in 17 h, while 66 h of incubation were needed to achieve ≥95% digestion of the cross-linked complex. The digestion reaction was terminated by the addition of 0.5% (v/v) trifluoroacetic acid. We also performed double digestion of the cross-linked complex using GluC followed by AspN, which cleaves at the N terminus of aspartic acid residues and, at a slower rate, glutamic acid residues. The GluC-digested complex was further digested with 0.25 μg (w/v) endoproteinase AspN (Roche Diagnostics/Sigma) in 25 mM Tris-HCl, pH 8.1, 0.0002% (v/v) Zwittergent 3-16 detergent, at 37 °C overnight, followed by addition of 0.5% (v/v) trifluoroacetic acid. The cross-linked peptides were identified at the Mayo Clinic Proteomics Core by nano-flow liquid chromatography electrospray tandem mass spectrometry (MS/MS) using an Orbitrap Elite mass spectrometer (Thermo Fisher Scientific) coupled to a Thermo Ultimate 3000 RSLCnano HPLC system as described previously (32). Two independent GluC-digested complex preparations were subjected to chemical cross-linking and limited proteolysis as described above. In each case, the sample was analyzed by MS/MS both in the absence of any further treatment and after treatment with the reducing agent, tris(2-carboxyethyl)phosphine, at a final concentration of 50 mM at 60 °C for 30 min (Hampton Research). In addition, a third cross-linked complex digested with both GluC and AspN was analyzed by MS/MS after treatment with tris(2-carboxyethyl)phosphine as described above.

Analysis of Cross-linked Peptides—We used the StavroX 3.5.1 program (73) to generate a list of cross-linked peptides, including cross-links between FXN and ISCU, FXN and NFS1, FXN and ISD11, NFS1 and ISCU, and NFS1 and ISD11, and cross-links within FXN, ISCU, NFS1, or ISD11 from the five independent MS/MS analyses described above, as reported previously (32). Based on the amino acid sequences of FXN, ISCU, NFS1, and ISD11, the molecular weight and amino acid specificity of BS^3, and the cleavage specificity of GluC and AspN, the software calculated all theoretical possible combinations of cross-linked peptides and compared them with the precursor peptide masses in the MS file (73). Each identified cross-linked peptide was assigned a score based on a comparison between the theoretical fragmentation and the actual MS/MS spectrum of the cross-linked peptide (73). The software also calculated the FDR by comparing the number of candidates in each experimental dataset with the number of false-positive candidates from a decoy dataset, created from the inverted amino acid sequences of FXN, ISCU, NFS1, and ISD11. For each of five independent datasets, the software calculated a score range and the corresponding FDR values for all of the cross-linked peptides, which are shown in Table 2 and supplemental Table S2. Protein-protein distances were measured between each possible pair of cross-linked residues within each of the identified cross-linked peptides in the simulated structure of the $[FXN^{42-210}]_{12}\cdot[ISCU]_{12}\cdot[NFS1]_{12}$ sub-complex using a script (distance :resi#1.subunit#1@CA:resi#2.subunit#2@CA) in the command line of Chimera (46), and the mean distance ± S.D. was calculated for each possible pair of cross-linked residues, as reported previously (supplemental Table S2) (32). For ISD11 cross-links, distances were measured in the simulated half-structure with modeled ISD11 monomers. Because BS^3 has a space arm of 11.4 Å, the distance constraint between the backbone α-carbons of two cross-linked residues was assumed to be equal to the length of the BS^3 spacer arm + the lengths of the side chains of the two cross-linked residues. The distance constraints for all of the possible pairs of residues that can be cross-linked by BS^3 are shown in the legend of supplemental Table S2, and distances ± S.D. measured in the structure that are equal to or lower than the distance constraints are highlighted in light gray in the table. In addition, the maximum allowable distance constraint between the backbone α-carbons of two cross-linked residues was assumed equal to the distance constraint plus the estimated resolution-dependent errors (74) in the positions of FXN^{42-210}, ISCU, NFS1, or ISD11 protein atoms. The resolution-dependent errors (RDE) for FXN^{42-210}-ISCU (9.0 Å), FXN^{42-210}-FXN^{42-210} (10.2 Å), FXN^{42-210}-NFS1 (9.0 Å), FXN^{42-210}-ISD11 (8.6 Å), ISCU-ISCU (7.8 Å), ISCU-NFS1 (7.8 Å), ISCU-ISD11 (7.4 Å), NFS1-NFS1 (7.8 Å), and NFS1-ISD11 (7.4 Å) were calculated from the resolution of the $Yfh1^{Y73A}$ trimer crystal structure (PDB code 3OEQ; RDE = 5.1 Å) used for homology modeling of FXN^{42-210}, the resolution of the crystal structures of *A. fulgidus* IscU (PDB code 4EB5; RDE = 3.9 Å), and *E. coli* IscS (PDB code 3LVJ; RDE = 3.9 Å), which were used for I-TASSER homology modeling of ISCU and NFS1, respectively, and the resolution of the structure of an uncharacterized protein from *Deinococcus radiodurans* (3GW4; RDE = 3.5 Å), identified by I-TASSER as a probable structural homologue of ISD11. Distances measured in the simulated half-structure that are equal to or lower than the maximum allowable distance constraints are highlighted in dark gray in supplemental Table S2; all greater distances are highlighted in yellow.

Analysis of Complex Interfaces—A coordinate file of the active center of the four-protein complex, $[FXN^{42-210}]_6\cdot[NFS1]_2\cdot[ISCU]_6$, was extracted from the simulated half-structure of the complex and was uploaded into the PISA program. The PISA Interfaces algorithm was used to identify FXN-FXN, ISCU-ISCU, NFS1-NFS1, FXN-ISCU, FXN-NFS1, and ISCU-NFS1 interfaces and buried surface areas thereof.

Electrostatic Potential Calculation—The coordinate files of the $[FXN^{42-210}]_3$, $[ISCU]_3$, $[FXN^{42-210}]_3\cdot[ISCU]_3$, $[FXN^{42-210}]_6\cdot[ISCU]_6$, and $[NFS1]_2$ sub-complexes were extracted from the simulated half-structure of the complex and uploaded into the PDB2PQR server, and the electrostatic surface potential was calculated for each sub-complex using the Poisson-Boltzmann equation. The Adaptive Poisson-Boltzmann Solver (APBS) software package was used to visualize protein surfaces in the PyMOL program.

Author Contributions—O. G. and W. R. contributed equally to the execution of all experiments, wrote the initial draft of the paper, and prepared the figures. E. C. A. helped with the development of the EM protocol. D. Y. S. provided technical assistance with complex isolation and biochemical characterization. S. A. K. and J. R. T. contributed to the structural analysis of the complex and revised the paper. G. I. coordinated the study, revised the paper, and contributed to the preparation of the figures. All authors analyzed the results and approved the final version of the manuscript.

Acknowledgments—We thank Drs. R. Hafner (Characterization Facility, College of Science and Engineering, University of Minnesota) and W. Zang (Department of Diagnostic and Biological Sciences, School of Dentistry, University of Minnesota) for training and assisting in performing transmission EM; B. Madden (Proteomics Core, Mayo Clinic, Rochester, MN) for MS/MS data collection; J. Charlesworth (Microscopy and Cell Analysis Core, Mayo Clinic, Rochester, MN) for technical help; and Dr. S. Ludtke (Baylor College of Medicine) and the EMAN2 Discussion List for helpful suggestions.

References

1. Lill, R., Hoffmann, B., Molik, S., Pierik, A. J., Rietzschel, N., Stehling, O., Uzarska, M. A., Webert, H., Wilbrecht, C., and Mühlenhoff, U. (2012) The role of mitochondria in cellular iron-sulfur protein biogenesis and iron metabolism. *Biochim. Biophys. Acta* **1823,** 1491–1508
2. Kim, J. H., Bothe, J. R., Alderson, T. R., and Markley, J. L. (2015) Tangled web of interactions among proteins involved in iron-sulfur cluster assembly as unraveled by NMR, SAXS, chemical crosslinking, and functional studies. *Biochim. Biophys. Acta* **1853,** 1416–1428
3. Blanc, B., Gerez, C., and Ollagnier de Choudens, S. (2015) Assembly of Fe/S proteins in bacterial systems: biochemistry of the bacterial ISC system. *Biochim. Biophys. Acta* **1853,** 1436–1447
4. Maio, N., and Rouault, T. A. (2015) Iron-sulfur cluster biogenesis in mammalian cells: New insights into the molecular mechanisms of cluster delivery. *Biochim. Biophys. Acta* **1853,** 1493–1512
5. Layer, G., Ollagnier-de Choudens, S., Sanakis, Y., and Fontecave, M. (2006) Iron-sulfur cluster biosynthesis: characterization of *Escherichia coli* CyaY as an iron donor for the assembly of [2Fe-2S] clusters in the scaffold IscU. *J. Biol. Chem.* **281,** 16256–16263
6. Li, H., Gakh, O., Smith, D. Y., 4th, and Isaya, G. (2009) Oligomeric yeast frataxin drives assembly of core machinery for mitochondrial iron-sulfur cluster synthesis. *J. Biol. Chem.* **284,** 21971–21980
7. Gakh, O., Bedekovics, T., Duncan, S. F., Smith, D. Y., 4th, Berkholz, D. S., and Isaya, G. (2010) Normal and Friedreich ataxia cells express different isoforms of frataxin with complementary roles in iron-sulfur cluster assembly. *J. Biol. Chem.* **285,** 38486–38501
8. Cook, J. D., Kondapalli, K. C., Rawat, S., Childs, W. C., Murugesan, Y., Dancis, A., and Stemmler, T. L. (2010) Molecular details of the yeast frataxin-Isu1 interaction during mitochondrial Fe-S cluster assembly. *Biochemistry* **49,** 8756–8765
9. Bridwell-Rabb, J., Iannuzzi, C., Pastore, A., and Barondeau, D. P. (2012) Effector role reversal during evolution: the case of frataxin in Fe-S cluster biosynthesis. *Biochemistry* **51,** 2506–2514
10. Pandey, A., Gordon, D. M., Pain, J., Stemmler, T. L., Dancis, A., and Pain, D. (2013) Frataxin directly stimulates mitochondrial cysteine desulfurase by exposing substrate-binding sites, and a mutant Fe-S cluster scaffold protein with frataxin-bypassing ability acts similarly. *J. Biol. Chem.* **288,** 36773–36786
11. Webert, H., Freibert, S. A., Gallo, A., Heidenreich, T., Linne, U., Amlacher, S., Hurt, E., Mühlenhoff, U., Banci, L., and Lill, R. (2014) Functional reconstitution of mitochondrial Fe/S cluster synthesis on Isu1 reveals the involvement of ferredoxin. *Nat. Commun.* **5,** 5013
12. Tsai, C. L., and Barondeau, D. P. (2010) Human frataxin is an allosteric switch that activates the Fe-S cluster biosynthetic complex. *Biochemistry* **49,** 9132–9139
13. Colin, F., Martelli, A., Clémancey, M., Latour, J. M., Gambarelli, S., Zeppieri, L., Birck, C., Page, A., Puccio, H., and Ollagnier de Choudens, S. (2013) Mammalian frataxin controls sulfur production and iron entry during *de novo* Fe_4S_4 cluster assembly. *J. Am. Chem. Soc.* **135,** 733–740
14. Vaubel, R. A., and Isaya, G. (2013) Iron-sulfur cluster synthesis, iron homeostasis and oxidative stress in Friedreich ataxia. *Mol. Cell. Neurosci.* **55,** 50–61
15. Cavadini, P., Adamec, J., Taroni, F., Gakh, O., and Isaya, G. (2000) Two-step processing of human frataxin by mitochondrial processing peptidase. Precursor and intermediate forms are cleaved at different rates. *J. Biol. Chem.* **275,** 41469–41475
16. Schmucker, S., Argentini, M., Carelle-Calmels, N., Martelli, A., and Puccio, H. (2008) The *in vivo* mitochondrial two-step maturation of human frataxin. *Hum. Mol. Genet.* **17,** 3521–3531
17. Jobling, R. K., Assoum, M., Gakh, O., Blaser, S., Raiman, J. A., Mignot, C., Roze, E., Dürr, A., Brice, A., Lévy, N., Prasad, C., Paton, T., Paterson, A. D., Roslin, N. M., Marshall, C. R., *et al.* (2015) PMPCA mutations cause abnormal mitochondrial protein processing in patients with non-progressive cerebellar ataxia. *Brain* **138,** 1505–1517
18. Schmucker, S., Martelli, A., Colin, F., Page, A., Wattenhofer-Donzé, M., Reutenauer, L., and Puccio, H. (2011) Mammalian frataxin: an essential function for cellular viability through an interaction with a preformed ISCU/NFS1/ISD11 iron-sulfur assembly complex. *PLoS One* **6,** e16199
19. Li, H., Gakh, O., Smith, D. Y., 4th, Ranatunga, W. K., and Isaya, G. (2013) Missense mutations linked to Friedreich ataxia have different but synergistic effects on mitochondrial frataxin isoforms. *J. Biol. Chem.* **288,** 4116–4127
20. Shi, R., Proteau, A., Villarroya, M., Moukadiri, I., Zhang, L., Trempe, J. F., Matte, A., Armengod, M. E., and Cygler, M. (2010) Structural basis for Fe-S cluster assembly and tRNA thiolation mediated by IscS protein-protein interactions. *PLoS Biol.* **8,** e1000354
21. Marinoni, E. N., de Oliveira, J. S., Nicolet, Y., Raulfs, E. C., Amara, P., Dean, D. R., and Fontecilla-Camps, J. C. (2012) $(IscS\text{-}IscU)_2$ complex structures provide insights into Fe_2S_2 biogenesis and transfer. *Angew. Chem. Int. Ed. Engl.* **51,** 5439–5442
22. Prischi, F., Konarev, P. V., Iannuzzi, C., Pastore, C., Adinolfi, S., Martin, S. R., Svergun, D. I., and Pastore, A. (2010) Structural bases for the interaction of frataxin with the central components of iron-sulphur cluster assembly. *Nat. Commun.* **1,** 95
23. Bridwell-Rabb, J., Fox, N. G., Tsai, C. L., Winn, A. M., and Barondeau, D. P. (2014) Human frataxin activates Fe-S cluster biosynthesis by facilitating sulfur transfer chemistry. *Biochemistry* **53,** 4904–4913
24. Fox, N. G., Das, D., Chakrabarti, M., Lindahl, P. A., and Barondeau, D. P. (2015) Frataxin accelerates [2Fe-2S] cluster formation on the human Fe-S assembly complex. *Biochemistry* **54,** 3880–3889
25. Parent, A., Elduque, X., Cornu, D., Belot, L., Le Caer, J. P., Grandas, A., Toledano, M. B., and D'Autréaux, B. (2015) Mammalian frataxin directly enhances sulfur transfer of NFS1 persulfide to both ISCU and free thiols. *Nat. Commun.* **6,** 5686
26. Amela, I., Delicado, P., Gómez, A., Querol, E., and Cedano, J. (2013) A dynamic model of the proteins that form the initial iron-sulfur cluster biogenesis machinery in yeast mitochondria. *Protein J.* **32,** 183–196
27. Adamec, J., Rusnak, F., Owen, W. G., Naylor, S., Benson, L. M., Gacy, A. M., and Isaya, G. (2000) Iron-dependent self-assembly of recombinant yeast frataxin: implications for Friedreich ataxia. *Am. J. Hum. Genet.* **67,** 549–562
28. Söderberg, C. A., Rajan, S., Shkumatov, A. V., Gakh, O., Schaefer, S., Ahlgren, E. C., Svergun, D. I., Isaya, G., and Al-Karadaghi, S. (2013) The molecular basis of iron-induced oligomerization of frataxin and the role of the ferroxidation reaction in oligomerization. *J. Biol. Chem.* **288,** 8156–8167
29. Gakh, O., Smith, D. Y., 4th, and Isaya, G. (2008) Assembly of the iron-binding protein frataxin in *Saccharomyces cerevisiae* responds to dynamic

changes in mitochondrial iron influx and stress level. *J. Biol. Chem.* **283,** 31500–31510

30. Seguin, A., Sutak, R., Bulteau, A. L., Garcia-Serres, R., Oddou, J. L., Lefevre, S., Santos, R., Dancis, A., Camadro, J. M., Latour, J. M., and Lesuisse, E. (2010) Evidence that yeast frataxin is not an iron storage protein *in vivo*. *Biochim. Biophys. Acta* **1802,** 531–538
31. Karlberg, T., Schagerlöf, U., Gakh, O., Park, S., Ryde, U., Lindahl, M., Leath, K., Garman, E., Isaya, G., and Al-Karadaghi, S. (2006) The structures of frataxin oligomers reveal the mechanism for the delivery and detoxification of iron. *Structure* **14,** 1535–1546
32. Ranatunga, W., Gakh, O., Galeano, B. K., Smith, D. Y., 4th, Söderberg, C. A., Al-Karadaghi, S., Thompson, J. R., and Isaya, G. (2016) Architecture of the yeast mitochondrial iron-sulfur cluster assembly machinery: the sub-complex formed by the iron donor, Yfh1, and the scaffold, Isu1. *J. Biol. Chem.* **291,** 10378–10398
33. Schagerlöf, U., Elmlund, H., Gakh, O., Nordlund, G., Hebert, H., Lindahl, M., Isaya, G., and Al-Karadaghi, S. (2008) Structural basis of the iron storage function of frataxin from single-particle reconstruction of the iron-loaded oligomer. *Biochemistry* **47,** 4948–4954
34. Bedekovics, T., Gajdos, G. B., Kispal, G., and Isaya, G. (2007) Partial conservation of functions between eukaryotic frataxin and the *Escherichia coli* frataxin homolog CyaY. *FEMS Yeast Res.* **7,** 1276–1284
35. Saha, P. P., Srivastava, S., Kumar S K P, Sinha, D., and D'Silva, P. (2015) Mapping key residues of ISD11 critical for NFS1-ISD11 subcomplex stability: implications in the development of mitochondrial disorder, COXPD19. *J. Biol. Chem.* **290,** 25876–25890
36. O'Neill, H. A., Gakh, O., and Isaya, G. (2005) Supramolecular assemblies of human frataxin are formed via subunit-subunit interactions mediated by a non-conserved amino-terminal region. *J. Mol. Biol.* **345,** 433–439
37. Wiedemann, N., Urzica, E., Guiard, B., Müller, H., Lohaus, C., Meyer, H. E., Ryan, M. T., Meisinger, C., Mühlenhoff, U., Lill, R., and Pfanner, N. (2006) Essential role of Isd11 in mitochondrial iron-sulfur cluster synthesis on Isu scaffold proteins. *EMBO J.* **25,** 184–195
38. Marelja, Z., Stöcklein, W., Nimtz, M., and Leimkühler, S. (2008) A novel role for human Nfs1 in the cytoplasm: Nfs1 acts as a sulfur donor for MOCS3, a protein involved in molybdenum cofactor biosynthesis. *J. Biol. Chem.* **283,** 25178–25185
39. Neuhoff, V., Stamm, R., Pardowitz, I., Arold, N., Ehrhardt, W., and Taube, D. (1990) Essential problems in quantification of proteins following colloidal staining with Coomassie Brilliant Blue dyes in polyacrylamide gels, and their solution. *Electrophoresis* **11,** 101–117
40. Andrews, P. (1965) The gel-filtration behaviour of proteins related to their molecular weights over a wide range. *Biochem. J.* **96,** 595–606
41. Hagel, L., Ostberg, M., and Andersson, T. (1996) Apparent pore size distributions of chromatography media. *J. Chromatogr. A* **743,** 33–42
42. Tang, G., Peng, L., Baldwin, P. R., Mann, D. S., Jiang, W., Rees, I., and Ludtke, S. J. (2007) EMAN2: an extensible image processing suite for electron microscopy. *J. Struct. Biol.* **157,** 38–46
43. Winn, M. D., Ballard, C. C., Cowtan, K. D., Dodson, E. J., Emsley, P., Evans, P. R., Keegan, R. M., Krissinel, E. B., Leslie, A. G., McCoy, A., McNicholas, S. J., Murshudov, G. N., Pannu, N. S., Potterton, E. A., Powell, H. R., *et al.* (2011) Overview of the CCP4 suite and current developments. *Acta Crystallogr. D Biol. Crystallogr.* **67,** 235–242
44. Ludtke, S. J. (2010) 3-D structures of macromolecules using single-particle analysis in EMAN. *Methods Mol. Biol.* **673,** 157–173
45. van Heel, M., and Schatz, M. (2005) Fourier shell correlation threshold criteria. *J. Struct. Biol.* **151,** 250–262
46. Pettersen, E. F., Goddard, T. D., Huang, C. C., Couch, G. S., Greenblatt, D. M., Meng, E. C., and Ferrin, T. E. (2004) UCSF Chimera–a visualization system for exploratory research and analysis. *J. Comput. Chem.* **25,** 1605–1612
47. Trabuco, L. G., Villa, E., Schreiner, E., Harrison, C. B., and Schulten, K. (2009) Molecular dynamics flexible fitting: a practical guide to combine cryo-electron microscopy and X-ray crystallography. *Methods* **49,** 174–180
48. Chan, K. Y., Gumbart, J., McGreevy, R., Watermeyer, J. M., Sewell, B. T., and Schulten, K. (2011) Symmetry-restrained flexible fitting for symmetric EM maps. *Structure* **19,** 1211–1218
49. Leitner, A., Walzthoeni, T., Kahraman, A., Herzog, F., Rinner, O., Beck, M., and Aebersold, R. (2010) Probing native protein structures by chemical cross-linking, mass spectrometry, and bioinformatics. *Mol. Cell. Proteomics* **9,** 1634–1649
50. Manicki, M., Majewska, J., Ciesielski, S., Schilke, B., Blenska, A., Kominek, J., Marszalek, J., Craig, E. A., and Dutkiewicz, R. (2014) Overlapping binding sites of the frataxin homologue assembly factor and the heat shock protein 70 transfer factor on the Isu iron-sulfur cluster scaffold protein. *J. Biol. Chem.* **289,** 30268–30278
51. Krissinel, E., and Henrick, K. (2007) Inference of macromolecular assemblies from crystalline state. *J. Mol. Biol.* **372,** 774–797
52. Bridwell-Rabb, J., Winn, A. M., and Barondeau, D. P. (2011) Structure-function analysis of Friedreich's ataxia mutants reveals determinants of frataxin binding and activation of the Fe-S assembly complex. *Biochemistry* **50,** 7265–7274
53. Majewska, J., Ciesielski, S. J., Schilke, B., Kominek, J., Blenska, A., Delewski, W., Song, J. Y., Marszalek, J., Craig, E. A., and Dutkiewicz, R. (2013) Binding of the chaperone Jac1 protein and cysteine desulfurase Nfs1 to the iron-sulfur cluster scaffold Isu protein is mutually exclusive. *J. Biol. Chem.* **288,** 29134–29142
54. Ramelot, T. A., Cort, J. R., Goldsmith-Fischman, S., Kornhaber, G. J., Xiao, R., Shastry, R., Acton, T. B., Honig, B., Montelione, G. T., and Kennedy, M. A. (2004) Solution NMR structure of the iron-sulfur cluster assembly protein U (IscU) with zinc bound at the active site. *J. Mol. Biol.* **344,** 567–583
55. Shimomura, Y., Wada, K., Fukuyama, K., and Takahashi, Y. (2008) The asymmetric trimeric architecture of [2Fe-2S] IscU: implications for its scaffolding during iron-sulfur cluster biosynthesis. *J. Mol. Biol.* **383,** 133–143
56. Söderberg, C. A., Shkumatov, A. V., Rajan, S., Gakh, O., Svergun, D. I., Isaya, G., and Al-Karadaghi, S. (2011) Oligomerization propensity and flexibility of yeast frataxin studied by x-ray crystallography and small-angle x-ray scattering. *J. Mol. Biol.* **414,** 783–797
57. Hempstead, P. D., Hudson, A. J., Artymiuk, P. J., Andrews, S. C., Banfield, M. J., Guest, J. R., and Harrison, P. M. (1994) Direct observation of the iron binding sites in a ferritin. *FEBS Lett.* **350,** 258–262
58. Gakh, O., Park, S., Liu, G., Macomber, L., Imlay, J. A., Ferreira, G. C., and Isaya, G. (2006) Mitochondrial iron detoxification is a primary function of frataxin that limits oxidative damage and preserves cell longevity. *Hum. Mol. Genet.* **15,** 467–479
59. Bou-Abdallah, F., Adinolfi, S., Pastore, A., Laue, T. M., and Dennis Chasteen, N. (2004) Iron binding and oxidation kinetics in frataxin CyaY of *Escherichia coli*. *J. Mol. Biol.* **341,** 605–615
60. Kato, S., Mihara, H., Kurihara, T., Takahashi, Y., Tokumoto, U., Yoshimura, T., and Esaki, N. (2002) Cys-328 of IscS and Cys-63 of IscU are the sites of disulfide bridge formation in a covalently bound IscS/IscU complex: implications for the mechanism of iron-sulfur cluster assembly. *Proc. Natl. Acad. Sci. U.S.A.* **99,** 5948–5952
61. Gerber, J., Mühlenhoff, U., and Lill, R. (2003) An interaction between frataxin and Isu1/Nfs1 that is crucial for Fe/S cluster synthesis on Isu1. *EMBO Rep.* **4,** 906–911
62. Neupane, G. P., and Kim, D. M. (2009) Comparison of the effects of deferasirox, deferiprone, and deferoxamine on the growth and virulence of *Vibrio vulnificus*. *Transfusion* **49,** 1762–1769
63. Park, S., Gakh, O., O'Neill, H. A., Mangravita, A., Nichol, H., Ferreira, G. C., and Isaya, G. (2003) Yeast frataxin sequentially chaperones and stores iron by coupling protein assembly with iron oxidation. *J. Biol. Chem.* **278,** 31340–31351
64. Saha, P. P., Kumar, S. K., Srivastava, S., Sinha, D., Pareek, G., and D'Silva, P. (2014) The presence of multiple cellular defects associated with a novel G50E iron-sulfur cluster scaffold protein (ISCU) mutation leads to development of mitochondrial myopathy. *J. Biol. Chem.* **289,** 10359–10377
65. Tsai, C. L., Bridwell-Rabb, J., and Barondeau, D. P. (2011) Friedreich's ataxia variants I154F and W155R diminish frataxin-based activation of the iron-sulfur cluster assembly complex. *Biochemistry* **50,** 6478–6487

66. Tong, W. H., and Rouault, T. (2000) Distinct iron-sulfur cluster assembly complexes exist in the cytosol and mitochondria of human cells. *EMBO J.* **19,** 5692–5700
67. Yang, J., Yan, R., Roy, A., Xu, D., Poisson, J., and Zhang, Y. (2015) The I-TASSER Suite: protein structure and function prediction. *Nat. Methods* **12,** 7–8
68. Trabuco, L. G., Villa, E., Mitra, K., Frank, J., and Schulten, K. (2008) Flexible fitting of atomic structures into electron microscopy maps using molecular dynamics. *Structure* **16,** 673–683
69. Emsley, P., Lohkamp, B., Scott, W. G., and Cowtan, K. (2010) Features and development of Coot. *Acta Crystallogr. D Biol. Crystallogr.* **66,** 486–501
70. Chen, V. B., Arendall, W. B., 3rd, Headd, J. J., Keedy, D. A., Immormino, R. M., Kapral, G. J., Murray, L. W., Richardson, J. S., and Richardson, D. C. (2010) MolProbity: all-atom structure validation for macromolecular crystallography. *Acta Crystallogr. D Biol. Crystallogr.* **66,** 12–21
71. Kalkhof, S., and Sinz, A. (2008) Chances and pitfalls of chemical cross-linking with amine-reactive *N*-hydroxysuccinimide esters. *Anal. Bioanal. Chem.* **392,** 305–312
72. Mädler, S., Gschwind, S., and Zenobi, R. (2010) Role of arginine in chemical cross-linking with *N*-hydroxysuccinimide esters. *Anal. Biochem.* **398,** 123–125
73. Götze, M., Pettelkau, J., Schaks, S., Bosse, K., Ihling, C. H., Krauth, F., Fritzsche, R., Kühn, U., and Sinz, A. (2012) StavroX–a software for analyzing crosslinked products in protein interaction studies. *J. Am. Soc. Mass Spectrom.* **23,** 76–87
74. Blow, D. M. (2002) Rearrangement of Cruickshank's formulae for the diffraction-component precision index. *Acta Crystallogr. D Biol. Crystallogr.* **58,** 792–797
75. Moore, S. (1963) On the determination of cysteine and cysteic acid. *J. Biol. Chem.* **238,** 235–237